# High temperature spectral emissivity of glass and crystal-bearing basalts

Jonas Biren, Aneta Slodczyk, Joan Andújar, Leire del Campo, Lionel Cosson, Hao Li, Emmanuel Veron, Cécile Genevois, Sandra Ory, Muhammad Aufaristama

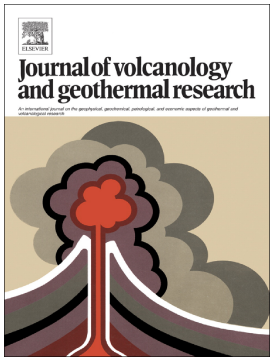


# High temperature spectral emissivity of glass and crystal-bearing basalts

Jonas Biren, Aneta Slodczyk, Joan Andújar, Leire del Campo, Lionel Cosson, Hao Li, Emmanuel Veron, Cécile Genevois, Sandra Ory, Muhammad Aufaristama

PII: S0377-0273(22)00154-8

DOI: https://doi.org/10.1016/j.jvolgeores.2022.107623

Reference: VOLGEO 107623

To appear in: *Journal of Volcanology and Geothermal Research*

Received date: 15 February 2022

Revised date: 27 June 2022

Accepted date: 30 June 2022

Please cite this article as: J. Biren, A. Slodczyk, J. Andújar, et al., High temperature spectral emissivity of glass and crystal-bearing basalts, *Journal of Volcanology and Geothermal Research* (2022), https://doi.org/10.1016/j.jvolgeores.2022.107623

# High temperature spectral emissivity of glass and crystal-bearing basalts.

Jonas Biren[a,*], Aneta Slodczyk[a,b], Joan Andújar[a], Leire del Campo[b], Lionel Cosson[b], Hao Li[a], Emmanuel Veron[b], Cécile Genevois[b], Sandra Ory[b], Muhammad Aufaristama[c]

[a]CNRS–Université d'Orléans, ISTO, BRGM, UMR 7327, F-45071, Orléans, France.
[b]CNRS–Université d'Orléans, CEMHTI, UPR 3079, F-45071, Orléans, France.
[c]University of Twente, ESA, Enschede, Netherlands.

[*]Corresponding author:
Jonas Biren
*Email address:* jonas.biren@cnrs-orleans.fr
*Postal address*: 1A, rue de la Férollerie, 45100 Orléans CEDEX 2

***Abstract***

Temperature is a key parameter controlling the rheology of lava flows. However, the unpredictable hazard of eruptions prevents direct measurements of hot volcanic bodies. Thus, the temperature of lava products is mostly retrieved by remote sensing techniques (ground- or satellite-based detectors) build on measuring infrared (IR) radiance. These well-established techniques are however subjected to important errors related to the poor knowledge of one of the most critical parameters, namely spectral emissivity. The aim of our study is to fill this gap by exploring the emissivity–temperature relationship of three different basalts. We performed *in situ* emissivity measurements at high temperatures (up to 1800 K) over a wide spectral range (350–8000 $cm^{-1}$; 1.25–28.6 µm), using a non-contact IR apparatus. To unravel the complex radiative behavior of the samples with temperature, structural, chemical and textural analyses using Raman spectroscopy, XRD, DSC, SEM, EMPA and TEM were systematically performed. Our results show that spectral emissivity varies with temperature, wavenumber, and the sample degree of polymerization combined with total FeO content. Spectral emissivity is greatly affected by the crystallization of Fe-Mg-rich crystals at the micro-scale. Consequently, this study proves that spectral emissivity cannot be assumed constant for a single magmatic composition. Finally, our laboratory-measured values of spectral emissivity allowed refining the remote sensing temperature of the 2014–2015 Holuhraun eruption (Bárðarbunga, volcano) by 50 K in average. These new insights will ultimately reduce uncertainties in temperature estimates based on IR technology, information that are crucial to improve hazard assessment in volcanic crisis.

***Keywords***

Emissivity / Temperature / FTIR / Remote Sensing / basalt / Bárðarbunga / Holuhraun

# 1 Introduction

Lava flows are one of the main hazards related to effusive basaltic volcanism as demonstrated in recent eruptions at Piton de la Fournaise on La Reunion Island (2007-2021; Chevrel et al. 2021), Bárðarbunga in Iceland (2014; Kolzenburg et al. 2017), Etna or Stromboli in Italy (2021; Fornaciai et al., 2021; ; Plank et al., 2019), Kilauea on Hawaii island (2014, 2018; Neal et al., 2019) and La Palma on Canary Islands (2021; Carracedo et al., 2022). For minimizing their impact on surrounding locations, it is strictly necessary to continuously monitor the propagation of the lava flows and accurately model their surface evolution for predicting their potential run-out distance (Harris et al., 2016). To this end, temperature (T) is one of the key parameters to be precisely determined, since it strongly controls the rheology of the progressing lava flow. This effect was well identified for the Bardanbunga eruption, where small temperature variations of ~50 K, induced the change from a highly fluid flow to a rheologically blocked lava (Giordano et al. 2007; Kolzenburg et al., 2018, 2017, 2016).

Lava temperature can be measured directly by thermocouples or indirectly via remote sensing (RS) instruments. However, the low representativeness and spatial coverage of the former along with the hazardous and unpredictable behavior of eruptions ensue that lava flows are more regularly monitored by ground-, air- and satellite-based remote sensing techniques (pyrometers, thermal cameras, and satellites). These techniques measure the emission flux (radiance) of the volcanic body at different wavelength ranges (Thermal InfraRed range, TIR, 8–14 μm; Mid InfraRed range, MIR, 3–5 μm; Short-Wave InfraRed range, SWIR, 1–2.5 μm; Aufaristama et al., 2019; Blackett, 2017; Ramírez-González et al., 2019; Rogic et al., 2019a), which is later converted into temperature using Planck's law.

Nevertheless, these well-established techniques are subjected to assumptions and limitations that can propagate important errors from measurements to derived eruptive parameters such as temperature (Harris, 2013; Thompson and Ramsey, 2021; Zakšek et al.,

2013). Measurements can be impacted by the variation of surrounding environment (e.g., atmospheric absorption, Gillespie et al. 1998; Harris 2013; Yang et al. 2020), and the constant changes in temperature, composition and texture of the cooling lava (e.g., Ramsey et al. 2019). Even if the uncertainties of environmental and of thermal gradients can be reduced, measuring emission flux, and determining temperature is ultimately challenging since today the variation of radiative properties of lava flow with temperature is poorly understood (e.g., Gillespie et al., 1998). Thus, the radiative properties of lava appear as the greatest source of inaccuracy for temperature retrieval (e.g., Zakšek et al. 2013).

In this framework, the aim of our study is to minimize the uncertainty in one of the hitherto poorly known and oversimplified parameters (e.g., Harris 2013; Rogic et al. 2019a), namely the spectral emissivity (ε). This parameter is crucial to invert remotely sensed data from lava flow's emission flux and to retrieve its temperature. To achieve this goal, we measured the evolution of the radiative properties of three different basaltic compositions using a direct IR emissivity measurement apparatus over a large range of temperatures (from room temperature up to 1800 K) and a wide spectral range (400–8000 $cm^{-1}$) covering TIR, MIR and SWIR. We then compare our results with the relevant literature and use them to refine the temperature of Holuhraun lava flow (Bárðarbunga volcano) derived by remote sensing technique.

### *1.1 Background on laboratory measurements of rock-magma emissivity.*

Spectral emissivity (ε) is the physical capacity of a material (e.g., lava flow) to emit heat radiation. The inner microscopic and macroscopic structure of the body (i.e., degree of polymerization; composition; presence of heterogeneities such as crystals and/or vesicles, and surface roughness) exerts an important control on phonon propagation and emissive behavior. Since magma composition and crystal content is strongly dependent on temperature (Andújar and Scaillet, 2012; Takeuchi, 2011), the progressive cooling and crystallization of an

evolving lava flow necessarily result in a continuous evolution of its radiative properties. Hence, to retrieve more precise temperature values using remote sensing techniques, it is necessary to have precise knowledge on the magma spectral emissivity.

Figure 1 shows an example of a broadband emissivity spectrum of a basaltic FeO-rich melted glass (Holuhraun eruption, Bárðarbunga) recorded at 1787 K. For better clarity, the part a) presents the characteristic spectral ranges: TIR–MIR–SWIR, and two specific bands: 10.9 µm and 1.6 µm, commonly used in the remote sensing application/community. Figure 1b shows three typical spectral regions that can be distinguished in the case of a dielectric material (e.g. silicate glass or melt; Howell et al., 2015):

1- The region <1500 $cm^{-1}$ (covering the TIR) reveals the main vibrations of a silicate network (e.g., $SiO_4$ tetrahedra). Since the absorption coefficient (K) is very high, the optical thickness (K × d, where d is sample thickness, here d = 3 mm) is great and the material appears opaque from the optical point of view in this spectral range. Two specific spectral features can be easily distinguished in the spectrum: the broad Reststrahlen band (centered at 980 $cm^{-1}$ and corresponding to the minimum value of emissivity) and Christiansen wavenumber or Christiansen Feature (CF), defined as the particular wavenumber (or wavelength) at which a dielectric material behaves as a perfect blackbody (ε = 1). The CF is specific for a given material and is commonly used for identification purpose (Ruff et al. 1997; Christensen et al. 2000; Cooper et al. 2002; King et al. 2004; Hamilton 2010) and to precisely determine the object temperature (Rozenbaum et al. 1999; De Sousa Meneses et al. 2015);

2- The spectral region between 1500 and 3500 $cm^{-1}$ (covering the MIR) is assigned to multiphonon processes. Since the absorption coefficient decreases almost exponentially in this region, a material appears semi-transparent from optical point of view. This leads to the significant decrease of the emissivity above 2000 $cm^{-1}$ and is

observed by presence of a Transmissivity Front (TF; De Sousa Meneses et al., 2015; Rozenbaum et al., 1999);

3- The spectral region >3500 $cm^{-1}$ (covering the SWIR and extended up to visible, VIS) is related to electronic processes (Rozenbaum et al. 1999; De Sousa Meneses et al. 2006). In the electronic region, most of materials such as pure silica appear transparent from an optical point of view. In the case of FeO-rich glass, the $Fe^{3+}$ or $Fe^{2+}$ absorptions detected in this spectral region, are responsible of high emissivity values.

The radiative properties of an object measured in the opaque region (TIR) are exclusively representative of its surface. On the contrary, the radiative properties recorded in the multiphonon and electronic regions (i.e. MIR and SWIR regions) are characteristic of the probed volume, which depends on optical thickness and then an object absorption coefficient (De Sousa Meneses et al. 2004).

Although ε is well studied at room and low temperatures (<353 K), there is today an apparent lack of spectral emissivity data for natural magmatic compositions recorded at high temperature conditions. In volcanology application, this lack of experimental data prompt to the default approach of using a constant ε value retrieved at room temperature for a given rock family (Crisp et al. 1990; Thomson and Salisbury 1993; Oppenheimer 1993; Harris and Thornber 1999; Calvari et al. 2005; Harris 2013; Chen et al. 2015; Ramsey et al. 2016; Kaneko et al. 2021; Thompson and Ramsey 2021). However, recent works (Rogic et al. 2019; Thompson and Ramsey 2020b; 2021) claim that this oversimplification neglects the effects of composition or temperature on the radiative properties of lava flow. For instance, large variations on emissivity (i.e., from 0.95 to 0.6) can under- or over-estimate the derived effective radiation temperature and impact the modeled runout distance of the lava flow by ~40 % (Rogic et al. 2019b; Ramsey et al., 2019). They recommend a tightly constrain on the

ε–T dependence for each magma composition over a wider spectral range (not only TIR) and at relevant magmatic temperatures (up to ~1500 K) as to select ε values adapted to the targeted volcanic material.

To date, few laboratory works addressed this issue with relative success (Bouvry et al., 2017; Lee et al., 2013; Lombardo et al., 2020; Rogic et al., 2019a; Thompson et al., 2021; Thompson and Ramsey, 2020) and their results highlight the non-linear relationship existing between emissivity and temperature (ε–T). However, most of these works are performed on crystals or synthetic glasses over a limited temperature and spectral range (typically the TIR region; Byrnes et al., 2007; Harris, 2013 and references therein; Lee et al., 2013; Pisello et al., 2019; Ramsey and Christensen, 1998; Rogic et al., 2019a). Moreover, the use of different apparatus having different set ups, sensibilities, loaded with synthetic compositions and different textures (e.g., rock powders, glassy materials), results in the production of a variable dataset of spectral emissivity values and contrasting ε–T relationships. For example, Abtahi et al., (2002), Lee et al., (2013) Pisello et al., (2019) Rogic et al., (2019a, b), Thompson et al., (2021) showed a negative ε–T relationship. Based on their observation, these authors state that the spectral emissivity of molten lava is lower than its solid counterpart. In contrast, the works of Bouvry et al., (2017), Lombardo et al., (2020), and Li et al. (2021) show rather constant or positive ε–T relationship over various spectral ranges, allowing the authors to state the contrary. The principal parameters they used, and the main results of their work are resumed in Table 1. This study shed light on the relation of spectral emissivity and temperature using broad analytical techniques described in the following section.

## 2 Methods

### *2.1 Starting materials preparation*

To assess the impact of mafic composition on the radiative properties, we selected three representative materials from different geological settings (Fig. 2a):

1- Icelandic scoriae and decametric lava samples from the 2014–2015 Holuhraun eruption (Bárðarbunga volcano) that were collected and kindly provided by A. Hoskuldsson (University of Iceland). The products from this event were selected since this eruption was one of the largest effusive episodes of the recent historical record of Iceland and Europe (Neave et al., 2019). At the same time, this was one of the first exceptional opportunity cases where it was possible to continuously monitor the changes in eruptive dynamic and temporal evolution of the eruption by aerial/satellite and ground based Infrared techniques (Nádudvari et al. 2020 and Aufaristama et al. 2018). Scoriae were retrieved at the crater site on October 14, 2014 and lava sample at ~1.1 km down flow from the crater location, on September 29, 2014 during the channel-fed lava emplacement (Pedersen et al., 2017).

2- Basanitic scoriae from the historical 1705 Fasnia eruption at Teide, Tenerife (named hereafter as "Fasnia") that were collected on the crater site in April 2017 (Albert et al. 2015). 3- Mid-Oceanic Ridge Basalt (named hereafter as MORB) that was collected at the Juan de Fuca ridge (Prouteau et al. 2001). The basanitic and MORB samples were selected as to study the effect of composition on the radiative properties of basaltic melts, since MORB closely approaches the composition of Bardarbunga basalt whereas the basanitic one, strongly differs from this for its alkaline rich-silica poor character (Table 2). Notwithstanding, since all the above samples are natural products containing different proportions of minerals and vesicles, all of them having specific radiative properties that will affect the sample's overall emissive response (Donaldson Hanna et al., 2012; Hamilton, 2010, 2000). In this study, all the samples were initially melted for obtaining homogeneous crystal-free glassy equivalents, that allowed us to strictly capture the effect of composition on ε alone without having any interference of

the crystal cargo.

Remelted glasses of Bárðarbunga (B-glass), Fasnia scoriae and Juan de Fuca MORB were prepared as follows: between 30 and 50 g of material were ground with agate mortar and pestle, and fused in a Pt crucible at 1720 K for 2h30 in open atmospheric conditions. The whole set was quenched in water, crushed, grounded and fused again at the same temperature for 1h30. The resulting melt was finally quenched in air. Fragments of the resulting starting glass were embedded in epoxy resin, polished and initially characterized with a Scanning Electron Microscope (SEM) to assess its homogeneity. Then the glasses were analyzed with electron microprobe (EMPA) for determining their composition and to ensure that no alkalis or iron migration from the sample to the Pt crucible occurred. Meanwhile, the glasses were drilled to recover cores with 10 mm diameter that were cut into 1.5±0.1 mm thick slices with parallel surfaces. The surface of each wafer was optically polished (Fig. 2b) to optimize the sample response during IR experiments at T<1500 K (De Sousa Meneses et al. 2015). Note, for IR measurements at higher temperatures (>1500 K), wafers with 3±0.1 mm thickness and 10 mm diameter were instead prepared. Finally, to explore the radiative properties of natural basaltic rocks and assess the impact of crystals on spectral emissivity, additional 1.5 and 3.0 mm wafers from natural not treated Bárðarbunga lava sample (named hereafter as "B-Nat") were prepared in the same way.

### *2.2 Experimental apparatus and procedure*

In order to determine the thermal radiative properties of the different basalts, two complementary methods of emissivity measurements can be applied: direct and indirect.

In the direct method, the spectral emissivity ($\varepsilon$) is defined as the ratio between the normal spectral radiance of the sample ($L$) and that of the blackbody ($L^0$) in the same thermal (temperature, T) and optical conditions (angle of measurement θ), (Boltzmann, 1884; Stefan, 1879):

$$\varepsilon(\sigma,T,\theta) = \frac{L(\sigma,T,\theta)}{L^0(\sigma,T,\theta)} \#(1)$$

The indirect method is based on second Kirchhoff's law where the spectral emissivity is indirectly derived from measurements of spectral reflectance (ρ) and spectral transmittance (τ), such as:

$$\varepsilon(\sigma,T,\theta) = 1 - \rho(\sigma,T,\theta) - \tau(\sigma,T,\theta) \#(2)$$

Note that for opaque materials with $\tau = 0$, $\varepsilon$ relies exclusively on ρ measurement.

Both methods have important advantages and drawbacks. The direct method allows to measure spectral emissivity up to very high temperatures (i.e., >2000 K; Rozenbaum et al. 1999), but at low temperatures (i.e., ≤500 K) only a limited spectral range, not exceeding 3000 $cm^{-1}$ (TIR–MIR), can be successfully measured by detector, Although, the indirect method gives access to wide spectral range (up to 8000 $cm^{-1}$, TIR–MIR–SWIR) at lower temperatures (<1000 K), it is impractical at temperatures >1000 K (Rozenbaum et al., 1999) because of the sample self-emission that hinders the reflection measurements and saturates the detector. Since the principal interest of this study is to measure the spectral emissivity of volcanic rocks up to molten conditions, we applied the direct method above 500 K. Indirect method allowing to deduce spectral emissivity from the transmissivity and reflectivity measurements was used at room temperature.

Evolution of ε with temperature (from 500 K until 1800 K) was measured *in situ* by using a non–contact spectral emittance apparatus developed at CEMHTI laboratory (Conditions Extrêmes et Matériaux : Haute Température et Irradiation, Orléans, France) (De Sousa Meneses et al., (2015). As shown in Figure 2d,e, the setup consists of a measuring chamber maintained at 295 K and purged continuously with dry air linked to two Fourier Transform InfraRed spectrometers (FTIR) set face-to-face. The chamber hosts a 180° rotating computer-controlled turntable, within which the sample is placed in front of the blackbody reference.

The latter is a Pyrox PY8 $LaCrO_3$ furnace with an aperture of 8 mm maintained at 1273 K for better stability. During measurements <1500 K, the sample is continuously heated with a 500 W $CO_2$ laser (Diamond K500, Coherent Inc.) which is divided into two equivalent beams as to heat the entire sample (1.5×10 mm) from above and below. This configuration allows creating a thermally homogeneous spot (no radial nor axial temperature gradients) on the center of the sample of 4 mm in diameter (Fig. 2c). In order to measure ε at T >1500 K, the 3×10 mm wafers were heated exclusively from above, since this configuration allows creating a small "fusion pond" at the surface of the sample, which works as a "self-crucible". The use of the $CO_2$ laser as a heating source allows avoiding thermal interferences that may arise when the sample is heated with a classical furnace. The only contribution is the characteristic $CO_2$ laser emission detected at ~940 $cm^{-1}$ (10.6 µm), which can be easily identified and eliminated from the signal, ensuring that only the emittance of the sample is considered.

The two face-to-face FTIR spectrometers are respectively a Vertex 70 (Bruker) purged with dry air and a Vertex 80v (Bruker) working under vacuum, set with multiple detectors and beam splitters (De Sousa Meneses et al. 2015) that allow to record the emittance in a wide spectral range from far IR to visible (50–20000 $cm^{-1}$). Such FTIR configuration allows simultaneous measurement of the sample and blackbody emittance (and inversely in the next rotation of the turntable) under the same environmental conditions. Note that in order to eliminate interferences from the apparatus environment itself, the thermal flux of the ambient background is also recorded.

When operating, the spectrometer diaphragms are set to 1 mm, which ensure a circular measuring spot of 2 mm in diameter within the 4 mm homogeneous thermal spot (Fig. 2c). The experimental configuration assures optimal measurement conditions in terms of environmental stability and single optical paths for the acquisition of thermal fluxes from

ambient to extreme temperatures (Rozenbaum et al. 1999; De Sousa Meneses et al. 2006; 2015). The resulting thermal emission signals include the sample signature, the blackbody as well as instrumentation and environment contributions that must be corrected. To eliminate these contributions, the method of three interferograms described by De Sousa Meneses et al., (2015) and derived from Planck law is applied. In this experimental procedure, we recorded three interferograms at each temperature, and then applied a Fourier transformation (TF) such as:

$$\varepsilon_\lambda = \frac{TF(I_s - I_a)}{TF(I_{bb} - I_a)} \frac{L^0_{bb} - L^0_a}{L^0_s - L^0_a} \#(2)$$

Where $I_a$, $I_{bb}$, $I_s$ are the interferograms (acquired with 64 scans) of the parasitic ambient contribution, the blackbody emission and the sample emission, respectively. Consequently, $L^0_a$, $L^0_{bb}$, $L^0_s$ are the Planck functions of the ambient, the blackbody and the sample. The respective thermal fluxes were collected every 50–100 K steps from 500 K to 1800 K (for a total of ~25 steps) and the sample was quenched afterwards by shutting the laser power down. Note that temperature is not straightforwardly set but is increased due to the laser power increase. The temperature value is then precisely radiometrically calculated (~98 % of accuracy, Brun 2003; Eckes et al. 2013) using the CF (Rozenbaum et al. 1999; De Sousa Meneses et al. 2015, Li et al. 2021). At this special wavenumber the FTIR spectrometer works as monochromatic pyrometer. A comparison with emittance values acquired by direct and indirect methods led us to estimate the standard uncertainty of ε measurements to be of 1–2 % at the vicinity of the CF and 5 % above 2000 $cm^{-1}$ (del Campo et al., 2011). Each measurement step takes ~15 minutes minimum, corresponding to the time necessary to achieve thermal equilibrium and to record the fluxes at the different rotation positions of the turntable. In consequence, the total duration of a single IR experiment can be estimated to ~8 h.

### *2.3 Additional sample characterization*

In order to understand the processes beyond the observed radiative properties of investigated basaltic samples, structural, textural, chemical, and thermal analyses were performed before and after *in situ* high temperature emissivity measurements, using the following experimental techniques.

#### 2.3.1 Scanning Electron Microscope and Electron Probe Micro Analyzer

Prior to analyses, sample chips were embedded in Epoxy resin, polished, and carbon coated (15–20 nm) under vacuum. Textural analysis was carried out with a Merlin Compact ZEISS Scanning Electron Microscope (FEG SEM) equipped with a GEMINI I column (15 kV, 10 mm working distance). Mineral and glass chemistry analyses were performed with an Electron Probe Micro Analyzer SXFive (EPMA) at 15 kV and 8 nA current using focused beam for minerals and 5, 10, 20 µm defocused beam for glass. Mineral end-members were calculated as in Deer et al. (2004) for olivine and plagioclase, and as in Morimoto (1988) for pyroxene.

#### 2.3.2 Transmission Electron Microscopy

Analysis of the experimental B-Glass sample by Transmission Electron Microscopy (TEM) helped in constraining the inner microstructure and composition after IR measurements. Two pieces were precisely extracted from the IR measuring area (Fig. 2c). Their cross sections were glued with their surfaces facing each other and then cut again to form a rectangle of ~2.5×2 mm (the so-called "sandwich" preparation; Ayache et al. 2007). The rectangular sample was mechanically polished with a tripod and inlaid diamond discs until a 50 µm thickness was reached. The resulting foil was finally obtained by argon ion milling (PIPS). Imaging, Selected Area Electron Diffraction (SAED) and TEM spectroscopy analyses were performed on a JEOL-ARM 200 Cold FEG transmission electron microscope operating at 80 kV, equipped with double spherical aberration correctors (TEM/STEM) and fitted with a

JEOL SDD CENTURIO EDS system and a Gatan Imaging Filter (GIF) Quantum ER. The microstructures of the sample surface and core were imaged by TEM bright field and Scanning Transmission Electron Microscopy – High Angle Annular Dark Field (STEM-HAADF) modes. Sample compositions (core and surface) were obtained with STEM-EDS (Energy Dispersive X-ray Spectroscopy) and STEM-EELS (Electron Energy Loss Spectroscopy). Changes in bonding, coordination or valence state are associated with the shape distribution of the energy-loss near-edge fine structure (ELNES) of core-loss edge like the $L_{2,3}$ transition metal and O–K near-edge. The ELNES data of our samples was then compared to those of sample with known structure (Colliex et al. 1991; Golla-Schindler et al. 2003, 2006).

2.3.3 Differential Scanning Calorimetry

Differential Scanning Calorimetry (DSC) analyses were carried out with a SETARAM Multi HTC 1600 in order to measure the glass transition temperature ($T_g$), and eventual crystallization events of synthesized glasses and natural basalts. Prior to the DSC analysis, the apparatus was calibrated against melting temperature of already known standards (gold, silver, aluminum), at different heating rates with a precision of 1 %. The glass and natural samples (500 mg of previously crushed and dried) were separately put in platinum crucible on the first thermocouple beam, whereas the platinum crucible on the second beam remained empty to work as a reference. Note that by definition, DSC measures the difference between heat flow rates of a sample and a reference material. The apparatus was first purged with Ar at a flow rate of 20 mL $min^{-1}$ and then, the predefined heating program was started (modified from Applegarth et al. 2013). The first program step, i.e. isotherm at 423 K and 15 min of equilibration, allowed eliminating oxygen/water traces from the furnace/sample and achieving the constant signal. A heating ramp with a constant rate of 10° $min^{-1}$ was then programmed to reach the temperature of 1723 K. Once this maximum temperature was

achieved, the cooling process with a constant rate 10° $min^{-1}$ allowed to decrease the T to 423 K. The sample was maintained at 423 K for 60 min in order to re-equilibrated the signal. Finally, the second heating-cooling cycle was recorded. The resulting differential heat flow curve showed the endothermic events as troughs, representative of temperature of the glass transition ($T_g$) and melting ($T_m$), and the exothermic events as peaks related to crystallization ($T_c$). $T_g$ was determined by taking the temperature at the intersection between the heat flow curve and the median line between both starting and ending glass transition temperatures. Note that melting under Ar gas has been usually identified in two endothermic events and crystallization in two to three exothermic events (Burkhard, 2001). The area of a peak or trough is directly proportional to the enthalpy of formation of each phase (Applegarth et al., 2013).

2.3.4 Raman spectroscopy

Raman spectroscopy gives insights into the local structural and chemical evolution of silicate glasses that can occur with temperature changes. Raman spectra were recorded *ex situ* prior and after IR experiments using a homemade micro-Raman apparatus equipped with a monochromatic 532 nm Coherent Genesis MX SLM laser as exciting source, a Nikon ECLIPSE Ni-U microscope, an Andor Shamrock 500i spectrometer equipped with an Edge filter cancelling intense Rayleigh elastic scattering and Peltier cooled back illuminated CCD Andor Newton detector. The use of long working distance Nikon objective (100×, N.A. 0.8) allowed micro-scale analysis with lateral resolution down to 1–2 $\mu m^2$. A 600 lines/mm grating was systematically used, providing spectral window spanning from 100 to 2700 $cm^{-1}$. For each analysis, acquisition time was set to 60 seconds and the laser power output varied between 100 and 300 mW. Daily calibration of the Raman micro-spectrometer was performed based on the 520.8 $cm^{-1}$ peak of silicon.

2.3.5 X-Rays Diffraction

*In situ* X-Rays Diffraction (XRD) measurements were performed in order to follow B-glass sample evolutions with temperature increase and to identify the nature of the crystalline/glassy phases present. High-temperature diffraction patterns were collected every 100 K from 873 K up to 1473 K using an Anton Paar oven chamber (HTK1200N model) in the 2θ range from 15 to 80° with a 0.021° step size and an acquisition time of 2 s per step. To avoid any textural effect (preferential orientation) after HT-XRD experiments, the sample was crushed and re-analyzed with the same parameters. Bragg peak identification for all phases was carried out in comparison with an extensive online database (PDF-4 edition 2021 from ICDD, https://www.icdd.com/, last accessed 02/02/22).

# 3 Results

## *3.1 Petrography of studied samples*

In order to retrieve the textural and chemical evolution of basalts after IR experiments, the petrography of each sample was first characterized.

### 3.1.1 Bárðarbunga sample

The composition of lava from Holuhraun eruption is basaltic with 48.91 wt. % $SiO_2$ and 2.73 wt. % alkalis (Mg# = 0.80) (Table 2). Bárðarbunga sample is vesicular and phenocryst-poor (crystals >1 mm and up to few cm), and contain microphenocrysts (0.1–1 mm) of plagioclase ($An_{67-87}$) as the dominant phase and lesser amounts of clinopyroxene ($Wo_{38-40}$ $En_{48}$ $Fs_{14-16}$, Mg# = 0.70–0.85 defined here as cations $\frac{Mg}{Mg+Fe^{2+}}$), olivine ($Fo_{69–76}$), and titanomagnetite ($Fe_2TiO_3$). The sample contains numerous microglomerocrysts of anhedral clinopyroxene, plagioclase, minor subhedral olivine and skeletal Fe-Ti oxides, and small vesicles (0.2–0.5 mm) set in a microlithic groundmass consisting of the same previous mineral assemblage. The identified textural and mineralogical features is similar to that of typical Icelandic tholeiites associated with the Bárðarbunga volcanic system as observed in Geiger et al. (2016) Kolzenburg et al. (2017), and Halldórsson et al. (2018).

### 3.1.2 Juan de Fuca MORB

The composition of the basalt from Juan de Fuca mid-oceanic ridge (Table 2) is similar to that described in Prouteau et al. (2001) and Mottl et al. (1994; Mg# = 0.59–0.73). This sample, called hereafter MORB, is very fine-grained, with crystal size <150 µm. Following the description of Mottl et al. (1994), olivine microphenocrysts morphology varies from partially rounded to euhedral with composition of $Fo_{77–86}$. Plagioclase microphenocrysts (~0.1 mm) are euhedral columnar crystals and have compositions ranging from $An_{88}$ to $An_{68}$. Clinopyroxene microphenocrysts are sub-euhedral and rounded, and are included in radiating aggregates with plagioclase. Fe-Ti oxides are skeletal individual and small (~0.01 mm), and

are associated with plagioclase and ferromagnesian grains (Mottl et al. 1994).

3.1.3 Fasnia sample (Tenerife, Canary Islands)

The composition of Fasnia eruption products can be classed as basanitic (Table 2) and is similar to those studied in Albert et al. (2015) and Jiménez-Mejías et al. (2021). Fasnia sample contains euhedral phenocrysts (13 wt. %; Albert et al., 2015) and microphenocrysts of olivine ($Fo_{87-79}$), clinopyroxene ($Wo_{48-50}$ $En_{35-41}$ $Fs_{12-14}$, Mg# = 72–78), Fe-Ti oxides of variable composition and plagioclase ($An_{69-51}$), the latter occurring only as microphenocrysts. The whole assemblage is set in a porphyritic texture with a fine-grained groundmass consisting of the same previous mineral assemblage and glass (Albert et al. 2015).

### *3.2 ε–T relationship for Bárðarbunga glass*

Figure S1 shows the temperature evolution of all recorded emissivity spectra for B-glass. As it can be clearly seen, five characteristic temperature intervals, in which the ε–T evolutions are very similar, can be distinguished. Consequently, for better readability Figure 3a (and all further Figures with spectral emissivity data of B-Nat (Fig. 3c), Fasnia (Fig. 4a) and MORB (Fig. 4c) presents the most representatives spectra from every characteristic temperature regions.

Figure 3a shows the spectral emissivity evolution with temperature for B-glass in the full investigated spectral range (TIR–MIR–SWIR, 400–8000 $cm^{-1}$) whereas Figure 3b is the zoom of the grey rectangle area visible in Figure 3a, and focuses on the TIR (400–2000 $cm^{-1}$) spectral range.

Below 1020 K (see the spectrum at 888 K in Figure 3a,b; Fig. S1), ε slightly varies with increasing temperature. In the spectral region <1500 $cm^{-1}$, the Reststrahlen bands reveals the vibrations of Si and Al-based tetrahedra of the disordered glass structure (Crisp et al. 1990; King et al. 2004). The CF is located at 1230 $cm^{-1}$ at ambient temperature while decreases to 1210 $cm^{-1}$ at 1020 K. The temperature evolution of the CF position is shown in Figure S2.

With the temperature increase (from 520K to 1020 K, Figure S1), ε minimum located at 980 $cm^{-1}$ slightly increases from 0.79 to 0.82, which is the expected evolution with temperature. Note that emissivity values retrieved in 917 $cm^{-1}$ (RS band 10.9 μm) and 6250 $cm^{-1}$ (RS band 1.6 μm) in all measured temperature steps are plotted in Figure S3. This behavior, comparable to that observed in pure silica (Rozenbaum et al., 1999), is related to the increasing dampening of the glass structure vibrations owing to the rise in anharmonicity and local structure reorganization. In the multiphonon region (between 1500–3500 $cm^{-1}$), the sample shows a transmissivity front (Fig. 1 and Fig. 3a) demonstrating that B-glass behaves as a semi-transparent material above CF. Therefore, the contribution of transmittance is not negligible, and the most commonly used method to estimate spectral emissivity based exclusively on reflectance measurements, i.e. "1-R" (Harris 2013), cannot be applied for B-glass and at any temperature.

Between 1020 and 1097 K (see the spectrum at 1097 K in Figure 3a,b; Figure S1), above the glass transition temperature, the ε markedly increases with temperature (from 0.94 close to unity, at 2400 $cm^{-1}$), making the transmissivity front indistinguishable. This rapid ε raise in multiphonon and electronic regions corresponds to an opacification phenomenon (Li et al., 2021 and references therein). In consequence, the material changes its optical properties from semi-transparent (ε is driven by volume scattering) to opaque (ε is driven by surface scattering only).

Between 1097 K and 1350 K (see the spectrum at 1264 K in Figure 3a,b, Figure S1), the temperature increase induces important changes in the ε behavior of the sample. In the TIR region, the wide Reststrahlen band splits into two distinct absorption peaks at ~850 $cm^{-1}$ and ~1030 $cm^{-1}$. These bands can be related to the presence of clinopyroxene crystals that have similar absorption bands at 900 and 1060 $cm^{-1}$ (exact band positions are affected by composition and slight difference in contribution of glass matrix). The CF shifts towards

smaller wavenumbers (i.e., from 1210 $cm^{-1}$ at 1097 K to 1080 $cm^{-1}$ at 1350 K, Figure S2) until it becomes undistinguishable above 1350 K. In the multiphonon and electronic regions (>1500 $cm^{-1}$), ε steadily decreases first and then oscillates between 0.90–0.94 in the temperature range 1200–1350 K (Fig. S1). These oscillations are related to the presence of large parabolic absorption bands that appear first at high wavenumbers and move towards lower wavenumbers as temperature increases. Such behavior, observed already in other materials (del Campo et al. 2008) reveals the presence of a layer of Fe-Mg-rich oxides demixing with the melting glass and clinopyroxene.

Between 1350 K and 1560 K (see the spectrum at 1560 K in Figure 3a,b, Figure S1) in the multiphonon and electronic regions, the temperature increase causes the collapse of the entire ε spectrum from ~0.93 to an almost invariable ε value of ~0.87 and the loss of the CF (Figs. S1-S3). Such significant modification of the emissivity points out to the complete segregation of the Fe-Mg-rich oxides to the sample surface. These Fe-Mg-rich oxides, having different optical properties than the glass, dominate the radiative response of B-glass. Because of the peculiar ε–T relationship observed at T >1350 K, the determination of the sample temperature using the CF wavenumber is no longer possible. Consequently, in order to retrieve the sample temperature, we assumed a flat spectrum having an emissivity level equivalent to that of reflectance spectrum measured after IR experiment on a sample which reached this temperature and was then cooled down before melting. Note that this method of temperature retrieval is not as much precise as that one based on the CF and can give T errors of ±30 K.

At 1654 K and above (Fig. 1, Fig. 3a,b, Fig. S1), the spectral signature is characterized by the presence of a broad Reststrahlen band in the opaque region (Rozenbaum et al., 1999) with a minimum at 980 $cm^{-1}$, and CF at 1210 $cm^{-1}$ (Fig. S2). It also shows a well-marked transmissivity front and almost constant ε value of ~0.87 in the electronic region.

These modifications reveal the complete melting of Fe-based oxides and ε is representative of B-glass molten state.

### *3.3 ε–T relationship for Bárðarbunga natural*

Figure 3c,d shows the spectral emissivity evolution with temperature for B-Nat. Note that vesicles strengthen the surface scattering and induce an ε increase in the opaque region compared to vesicle-free glass sample (Rozenbaum et al., 2009).

In the region of network vibrations (see the representative spectrum at 863 K in Figure 3c,d), one minor and two major absorption bands are located at ~530 $cm^{-1}$, and ~920 and ~1080 $cm^{-1}$ respectively. These bands can be related to the presence of clinopyroxene and plagioclase since these phases have characteristic absorptions at 515, 910 and 1070 $cm^{-1}$ (Donaldson Hanna et al., 2012; Hamilton, 2000) With temperature increase, the absorption bands slightly shift to 910 and 1050 $cm^{-1}$ (at 1256 K) before forming a single broad band above 1256 K, while their respective ε minimum increases from 0.80 to 0.86 and from 0.82 to 0.87. This overall behavior is the expected variation with temperature. Moreover, the CF initially located at 1246 $cm^{-1}$ at 863K, shifts to 1191 $cm^{-1}$ at 1648 K (Fig. S2.).

In the multiphonon and electronic regions, ε shows high values at low temperatures (e.g., ~0.97 at 2400 $cm^{-1}$ and 863 K) and no transmissivity front is observed. These spectral features differ from that of B-glass showing semi-transparent optical properties, implying that B-Nat is already opacified at low temperatures. This can be related to the initial organization of the silicate structure and the presence of Fe-Mg-rich crystals (= Fe-Mg-rich oxides + clinopyroxene) at ambient temperature. Their size (>500 nm) along with their high electric conductivity result in an important increase on sample ε despite their low concentration. With further temperature increase (T>1474 K), the sample becomes semi-transparent and the spectral emissivity plummets from ~0.98 (863 K) to ~0.85 (1648 K) in the multiphonon and electronic regions. As for B-glass, such progressive ε evolution can be associated with the

disorganization of B-Nat silicate structure through melting of the crystals and glass. Both samples, once fully molten (⩾1550 K), behave identically.

### *3.4 ε–T relationship for Fasnia and MORB*

In order to unravel the effect of composition on radiative properties of basalts, the ε–T relationship of Bárðarbunga glass (Table 3) was compared with those gained on a MORB from Juan de Fuca ridge and a basanite from Fasnia eruption (Tenerife, Canary Island) and gathered in Figure 4. Compared to B-glass radiative properties, MORB ε behaves similarly due to its close compositions (49.65 wt. % $SiO_2$, 3.04 wt. % alkali, Table 2). On the contrary, ε–T behavior of Fasnia is slightly different in agreement with its distinct composition (Table 2): Fasnia is more alkaline (44 wt. % $SiO_2$, 5.23 wt. % alkalis,) and has a lower FeO content (12.44 wt. %). The chemical differences are also confirmed by the CF values: 1228 and 1230 $cm^{-1}$ for MORB and Bárðarbunga respectively vs. 1215 $cm^{-1}$ in the case of Fasnia (Figs. 3,4, Fig. S2). This is in good agreement with the general statement that the more evolved the composition, the more polymerized the structure, and the shorter the wavelength at which the CF is observed (Pisello et al. 2019).

The temperature range, in which the opacification phenomenon appears, is the major difference between basalts and basanite glasses. In the case of MORB, ε jumps from 0.89 to 0.96 in the multiphonon region between 910 K and 990 K whereas Fasnia basanite is already opacified (with ε >0.95 in the multiphonon region) below 900 K. This difference was already observed in Bouvry et al. (2017) for other basaltic compositions. Note that MORB opacification occurs at lower temperature than B-glass (1020–1097 K).

With the temperature increase, MORB and Fasnia glasses show very similar ε–T evolution to B-glass (Fig. 4): first, they undergo crystallization of Fe-Mg-rich oxides and then their segregation from the silicate melt, The molten state is progressively reached at >1500 K. Spectral ε values do not notably vary from one sample to another at a given temperature (Fig.

4).

# 4 Discussion

## *4.1 High temperature radiative properties of basalts and origin of the opacification phenomenon*

The three basaltic glasses (B-glass, MORB, and Fasnia) studied in this work display similar emissivity evolution with temperature increase (Fig. 3 and Fig. 4). The main difference between their radiative behaviors is related to the temperature interval at which the opacification phenomenon is activated and thus when the optical properties change from semi-transparent to opaque. Opacification phenomenon is then characterized by very high values of spectral emissivity (>0.95) in the multiphonon and electronic regions. This thermally activated process, appearing as a jump-like emissivity increase has already been observed in our previous study on Fe-rich phonolites (Li et al. 2021) and attributed to the presence of Fe-ion clusters. Based on the results presented here for basalts, we further explored by means of complementary analyses (FTIR, SEM, EMPA, TEM, DSC, *ex situ* Raman spectroscopy and *in situ* XRD) the structural modifications (crystallization) which are responsible for the opacification phenomenon.

All experimental analyses reveal that starting B-glass is crystal-free and compositionally homogeneous (Fig. 5a). However, after the *in situ* ε measurements performed at T ≤1550 K the presence of crystals is confirmed in SEM and TEM (Fig. 5b and Fig. 6). In the sample core, there are ≤2 μm cubic Fe-rich oxides (bright phase in Fig. 5 and dark phase in Fig. 6a) along with early forms of clinopyroxene (augite) and plagioclase (light and dark grey, respectively, in Fig. 5b), set within a dark glassy matrix. In addition, the B-glass surface is characterized by the exolution of a newly formed Fe-Mg-rich crystalline layer of ~2 μm thick (Fig. 5b). Different Selected Area Electron Diffraction patterns in zone axis (SAED, insert in Fig. 6a) were indexed for several crystals at the sample surface and core in order to determine their structure in agreement with the chemical composition (Fig. 6b). Those at the surface can be classified as magnesioferrite [$Mg(Al_x, Fe^{3+}_{1-x})_2O_4$], with a cfc

(Fd-3m) structure and the cell parameter *a* of ~8.3 Å. Core crystals can be classified as iron oxides with a cfc (Fd-3m) structure (confirmed with XRD diffractograms) and the cell parameter *a* of ~8.4 Å. According to the ELNES fingerprints of the $L_{2,3}$ Fe edge, the core crystals exclusively contain $Fe^{3+}$ in their structure whereas the surface crystals contain $Fe^{3+}$ and Mg. Moreover, the ELNES fingerprint of the O–K edge of the core crystals corresponds to that of $\gamma$-$Fe_2O_3$ (maghemite), confirming the presence of this phase in the core of the sample.

In Fig. 7, the DSC heating–cooling cycles reveal that above temperature of glass transition, ($T_g$ = 939 K), two crystallization events can be identified with temperature increase in good agreement with *ex situ* Raman and *in situ* XRD results. A first exothermic peak ($T_c$) at 1132 K can be related to the crystallization of clinopyroxene and Fe-rich oxides, as suggested for Hawaiian basalts by Burkhard (2001). The second and less intense event ($T_c$) detected at 1370 K, points to further structure reorganization through crystallization of plagioclase. Raman spectra (Fig. 8a) clearly show the transformation of B-glass from homogeneous (glass only at 300 K before IR experiment) to heterogeneous (glass + crystals after IR experiment at 1780 K) state with the temperature increase. The new Raman peaks observed at 210, 287, 330 and 380 $cm^{-1}$, as well as more intense at 670 $cm^{-1}$ and 700 $cm^{-1}$ confirm the presence of clinopyroxene and Fe-Mg-rich oxides (Cáceres et al., 2021; Di Genova et al., 2018, 2016; Giordano et al., 2021; González-García et al., 2021; Huang et al., 2000; Lalla et al., 2016). The band at 700 $cm^{-1}$, assigned to the vibration of $Fe^{3+}$–O, is attributed to the formation of either Fe-Mg-rich oxides (Di Genova et al., 2020, 2017; Giordano et al., 2021), ferrite spinel or maghemite (γ-hematite, metastable; D'Ippolito et al., 2015; Zinin et al., 2011). *In situ* XRD analysis (Fig. 8b) allowed clarifying the presence of clinopyroxene (augite) and Fe-Mg-rich oxides ($Mg[Al_x, Fe^{3+}_{1-x}]_2O_4$, magnesioferrite) between 973 K and 1073 K; clinopyroxene being the dominant phase with higher absolute

intensity. The increasing intensity of Bragg peaks with temperature (Cullity, 1978) suggests that the Fe-Mg-rich oxide content progressively increases; hence its segregation towards the surface to form the crystalline layer is also progressive. It also concurs with the temperature at which the $Fe^{3+}$–O Raman band (700 $cm^{-1}$) becomes the dominant spectral feature (T>1360 K). The XRD diffractogram at 1473 K (Fig. 8b) is largely modified due to textural effects (e.g., preferential orientation) created by the coexistence of B-glass molten state and crystals. Raman spectroscopy and XRD analysis confirm the micro-scale crystallization of Fe-Mg-rich oxides and clinopyroxene, and their evolution (growing + fusion) with temperature increase.

Based on the above results, we can propose a sequence of events that accounts for the opacification phenomena in basaltic B-glass (Table 3). The progressing heating of the sample above $T_g$ induces the silicate glass anharmonicity increase and promotes the mobility of ions. This leads first to the microstructure re organization, then, above the glass transition temperature, to crystallization and growth of Fe-Mg-rich crystals and consequently ensues the sample opacification. It should be stressed that any temperature difference for crystallization and fusion events between the various techniques (IR, DSC, Raman, XRD) are related, on one side, to the starting material texture (powder vs. glass) and, on the other side to the heating history specific for each analytical device (furnace vs. laser, constant rate vs. quench). Nevertheless, the characteristic temperatures determined for each event agree within a reasonable interval (50–100 K).

Above 1150 K, the nucleation and crystallization of clinopyroxene occur along with the growth and the segregation of Fe-Mg-rich oxides from the melting glass towards the sample surface to form a Fe-rich micrometric layer (~2 μm; Fig. 5). Similar thin surface layer was already observed in del Campo et al. (2008) in the case of Fe-rich samples. They assigned the parabolic bands observed in emissivity spectra to the segregation between the

liquid and the forming iron-rich oxides. Moreover, they observed that the parabola maxima shift towards lower wavenumbers as the layer thickness grows. Thus, following their method, the oxide layer thickness in B-glass was estimated to be 0.3–1 μm depending on temperature, which is in accordance with SEM and TEM observations. Such crystal–melt segregation is also in good agreement with the works of Berger et al., (2019); Giuliani et al., (2020); Manylov et al., (2013). These authors claim that the heat treatment of basalt glass in air leads to complete iron oxidation and growth of magnesioferrite, which act as nucleation sites for pyroxene. Giordano et al., (2021); González-García et al., (2021), Mujin et al., (2021) also show the formation of Fe nanometric oxides and silicates at 1220–1320 K for rhyolitic melts. Cook et al. (1990) further demonstrate that oxidation occurs by the divalent cations ($Fe^{2+}$) diffusion from the interior of the glass to the free surface where they subsequently react with environmental oxygen to form a micrometric ($MgO[Fe^{3+}]_2O_4$) crystalline layer which covers the (divalent cation-depleted) glass. Thus, the sample radiative properties are first a mixed response from two distinct components: the near-molten glass and the Fe-Mg-rich oxides. With the temperature increase, this forming Fe-Mg-rich layer progressively controls the emissive behavior of B-glass sample. Moreover, once formed with irregular shape and thickness, it is responsible of the radical modification of IR spectra in the temperature range 1350–1550 K: an overall fall of ε values with no CF. This is due to the fact that Fe-Mg-rich oxides, with a high refractive index (~2) and behaving as electric conductors, have distinct radiative properties compared to those of the silicate melt and crystals (both dielectric). Their radiative properties do not involve a CF because the energy of their conduction electrons is more intense than that of the phonons (Howell et al., 2015). Therefore, Bárðarbunga radiative properties, driven by surface scattering, are exclusively governed by the Fe-Mg-rich oxides. Finally, starting from 1550 K the spectral signature of the Fe-Mg-rich oxides decreases significantly because of their melting, allowing the detection of typical spectrum of molten

silicate with characteristic CF. DSC and Raman results (Fig. 7, and Fig. 8) attest the melting of the Fe-Mg-rich oxides >1550 K.

In order to determine the effect of composition on the radiative properties of basaltic rocks, the B-glass results were then compared with those of MORB and Fasnia (Fig. 3, Fig. 4). The ε–T relationship of MORB is very similar to that of B-glass. Fasnia, instead, shows distinct radiative behavior. As it can be clearly seen in Figure 4, Fasnia glass is already opacified in the lowest measured temperatures whereas the opacification of MORB, similarly to the B-glass, is observed above $T_g$ (note $T_g$ temperatures: 934 and 939 K for MORB and Bárðarbunga respectively vs. 944 K for Fasnia; in good agreement with Bouhifd et al., (2013); Giordano et al., (2005); Robert et al., (2014). This is supported by Raman spectrum recorded at 300 K through the presence of the peak at ~670 $cm^{-1}$, meaning that the Fe-based clusters already exist at room temperature. It should be stressed that since Fasnia FeO content is lower than that in two other basalts (11.44 wt. % vs. >13 wt. %, Table 2), it cannot be fully responsible of the early opacification. Bearing in mind the chemical analysis in Table 2), it is clear that Fasnia is depleted in Si and enriched in alkalis (Na+K) compared to the two other basaltic counterparts. This means that basanitic sample silicate glass-melt network is initially more depolymerized in comparison with more evolved, polymerized Bárðarbunga and MORB. In consequence, Fasnia initial silicate structure allows faster ion diffusion, which makes the Fe-iron cluster formation much easier. To achieve similar microstructural state in the case of MORB and B-glass, high temperature activation is necessary. These results show clearly that the opacification phenomenon occurs in the magmatic rocks with high FeO content (>5 wt. %; Li et al. 2021) and changes their optical behavior (from semi-transparent to opaque). However, this process is enhanced by the degree of depolymerization of the system. This clearly indicates the high complexity of sample radiative properties and the necessity of careful lab-based measurements.

### *4.2 The effect of crystals on spectral emissivity: B-glass vs. B-Nat.*

We demonstrated that the spectral emissivity of crystallized natural basalt slightly differs from its glassy counterpart (Fig. 3). Since the natural sample (B-Nat) is a heterogeneous mixture of glass, crystals, and vesicles, each component exhibits specific radiative properties that will affect the sample's overall emissive response. It was previously demonstrated that small change in composition such as in mineral solid solution can give radically different radiative responses (Donaldson Hanna et al., 2012; Hamilton, 2010, 2000). Thus, the basalt radiative properties will differ depending on the crystal composition, size, content and distribution. Accordingly, they become more complex as more components are considered.

At low temperature (Fig. 3), the main difference between the emissive behavior of Bárðarbunga B-glass and B-Nat samples is related to the presence (or not) of a transmissivity front. Glass sample reveals the semi-transparent optical behavior whereas the crystalline counterpart shows opaque optical behavior (i.e., high emissivity) since the opacification phenomenon is already activated at these conditions. The presence of Mg-Fe-rich crystals (oxides + clinopyroxene) already at ambient temperature in the crystalline sample are responsible of such high emissivity. Their size (>5 µm) along with their proportion (B-Nat is richer than B-glass) result in the opacification phenomenon, as previously described. In contrast, the glassy counterpart reaches similar emissivity values at higher temperature, conditions at which crystals are formed with higher proportion than B-Nat as to compensate their smaller size (~2 µm). Moreover, at high melt fractions and low crystal proportions, the sample radiative properties would be dominated by the liquid even if small number of crystals are still present in the system (Fig. 5).

Another difference between both Bárðarbunga samples is the lack of segregation phenomenon in the case of B-Nat. This is evidenced by the fact that B-Nat sample never lose its CF, compared to B-glass at equivalent temperature range. This can be explained by the different kinetics and dynamics of the same processes (and similar emissivity value): B-glass

experiences crystallization whereas B-Nat experiences melting with temperature increase. This is why B-glass and B-Nat samples show relatively similar but not identical ε–T relationships.

Furthermore, we suggest that, although present in B-Nat matrix, other crystals (such as plagioclase and olivine) with lower emissivity in MIR-SWIR spectral regions (~0.20; Donaldson Hanna et al., 2012; Eckes et al., 2013; Ferrari et al., 2014) have smaller contribution to the sample radiative properties and are more sensible to volume scattering than crystals with high emissivity (e.g., augite ~0.80; Ferrari et al., 2014; Hamilton, 2000). For instance, the presence of Mg-Fe-rich oxides in basalts tends to increase the emissivity in the MIR–SWIR (opaque behavior) whereas the presence of olivine crystals tends to decrease the emissivity in MIR–SWIR (semi-transparent behavior. Consequently, the radiative properties of olivine-rich lava (e.g., the 2007 Piton de la Fournaise lava flow, La Réunion Island) will differ greatly from that of Bardarbunga lava.

In conclusion, the presence of crystals and their composition, relative proportion to melt / crystal phase exert an important control on the emissive response of basaltic lavas. Thus, the radiative properties of magmatic crystals are crucial to further understand the important differences in radiative properties in MIR–SWIR spectral regions.

### *4.3 Comparison with previous works*

Prior to this work, only handful studies investigated the high temperature radiative properties of basalts (Abtahi et al., 2002; Bouvry et al., 2017; Lombardo et al., 2020; Pisello et al., 2019; Rogic et al., 2019b, 2019a; Thompson et al., 2021). One of the most important achievements of our study is that the spectral emissivity of three different basaltic magmas was successfully recorded up to melting conditions and over a wide spectral range whereas previous works considering much lower temperatures were focused only on TIR spectral range. Although, we observed a similar ε–T relationship in multiphonon and electronic regions (MIR and SWIR) as Bouvry et al. (2017) and Thompson et al., (2021), the most

striking difference in respect to previous works is related to the evolution of emissivity with temperature in opaque region (TIR). Abtahi et al. (2002) and (Lee et al., 2010; Rogic et al., 2019b, 2019a; Thompson et al., 2021) determined high ε values (>0.8) for their basalts, but contrary to our results, they showed that spectral emissivity decreases with increasing temperature in TIR (Table 1). This negative ε–T relationship allowed the authors to state that the emissivity of molten lava is lower than that of their rock equivalent. It should be stressed that their conclusions were based on measurements performed at relatively low temperatures (900–1323 K). These authors did not attain full melting and extrapolated to high temperatures the emissivity values obtained at low temperatures, putting into question their assumption, and hence its applicability to real volcanic systems. Moreover, this assumption was later used by Ramsey et al. (2019) to study the effect of spectral emissivity on Tolbachik lava flow using PyFlowGo model (Chevrel et al., 2018). Without constrained data at high temperature, spectral emissivity have drastic impact on lava retrieved temperatures (and ultimately have important consequences on the final modeled distance-to-run of the flow (Ramsey et al., 2019; Rogic et al., 2019b).

### *4.4 Refining Holuhraun lava flow temperature*

We explore here the impact of emissivity measured in the laboratory on the RS retrieval of field temperature. At the time of eruption, few authors have constrained the temperature of the 2014–2015 Holuhraun lava flow field by applying different methodologies. Kolzenburg et al. (2017) estimated an average temperature of 1368 K (results range from 1355 to 1401 K) at the lava flow front during emplacement using thermocouple measurements. Simultaneously, they measured temperatures of freshly exposed lava using a FLIR T650 thermal camera (7.5–14 μm; 1353–1398 K) which are in good agreement with the direct thermocouple measurements, though no information was provided on spectral emissivity values used to determine temperature. Kolzenburg et al. (2017) also estimated the range of eruption temperature at the primary vent from 1420 to 1473 K, which concurs with Nádudvari et al.

(2020) high temperature calculation (1323–1333 K) using satellite images (Landsat-8 OLI in SWIR and ETM+ in NIR, SWIR) and multiple emissivity values (1.00, 0.93, and 0.80). Aufaristama et al. (2018) compared the results derived from satellite images (Landsat-8) using constant spectral emissivity (0.97) with field measurements. They show that these two temperature estimates agree for the molten component of the lava flow: satellite images yield temperature of 1369 K, whereas retrieved field measurement is 1320 K.

However, since these temperature estimates were retrieved by considering a constant ε value, in this section we use the ε–T relationships gained on the E-Nat data as to refine the previous temperatures using RS techniques. The results from this sample were preferred to those from B-glass, since the emissivity of the latter impacted by the segregation of iron-rich oxides, rendering data between 1350 and 1500 K unusable for modelisation (Fig. 3). In detail, we use our data to refine the pre-existing model of Aufaristama et al. (2018) at two spectral bands of interest for RS: SWIR (1.6 µm) and TIR (10.9 µm) (Fig. 9; Biren et al. 2021).

In the previous case, the authors calculated the radiance of a given pixel on the TIR and SWIR regions as:

$$R_{SWIR} = \frac{[L(\lambda_{SWIR}) - L_R(\lambda_{SWIR})]}{\tau\, \varepsilon_{SWIR}} \#(4)$$

And

$$R_{TIR} = \frac{[L(\lambda_{TIR}) - L_U(\lambda_{TIR})]}{\tau\, \varepsilon_{TIR}} \#(5)$$

where $R_{SWIR/TIR}$ are the corrected spectral radiances at wavelength $\lambda_{SWIR/TIR}$, respectively, $L(\lambda_{SWIR/TIR})$ are the spectral radiances at the sensor, $L_U$ is the atmospheric upwelling radiance, $L_R$ is the atmospheric reflected radiance, τ is atmospheric transmissivity, and ε is the surface emissivity. Then, as shown in Figure 9 we have mathematically regressed

the ε–T evolution of B-Nat obtained in this study at 1.6 and 10.9 µm to derive equations that consider the temperature and wavelength dependency of spectral emissivity (Fig. 9):

$$\varepsilon_{SWIR} = 0.586 + 7.123\ 10^{-4}\ \times T - 3.084\ 10^{-7} \#(6 \quad )$$

and

$$\varepsilon_{TIR} = 0.826 - 8.235\ 10^{-5}\ \times T + 7.818\ 10^{-8} \#(7)$$

these expressions replace the constant ε parameter in the radiance equation of Aufaristama et al 2018 and are solved for retrieving a new T value.

In regard to our results (spectral emissivity varies with temperature in broad band between 0.80–1.00), the assumed constant value of 0.97 can be considered as an overestimation of the real spectral emissivity of the lava flow. If the spectral emissivity of the lava flow is overestimated, then so too is the derived surface temperature measured by remote sensing techniques. By solving the above equations, the temperature we obtained using the refined model for the molten component is slightly lower (1325 K) than those determined by (1375 K) of Aufaristama et al. (2018) and (1420 K) of Kolzenburg et al. 2017. When the models of Aufaristama and ours are compared, the average absolute temperature difference for molten lava in the lava channel is ~50 K (Biren et al., 2021). Such temperature variation can infer great consequences on lava rheology as suggested in Andújar and Scaillet, (2012); and Kolzenburg et al., (2018). Accordingly, lab-based IR results when confronted to the field IR data help in increasing accuracy in temperature retrieval by Remote Sensing techniques. Moreover, these observations imply that lava is less likely to lose heat radiatively compared to the common use of constant emissivity (0.97). Consequently, lava flow takes longer time to dissipate its heat allowing longer distances to be reached. The latter modification increases ultimately the associated hazard, which is of utmost importance in the case of lava flow inundating inhabited area (e.g., the recent eruption at La Palma, Spain). Consecutively, our

new insights will help reduce the error related to thermo-rheological models of lava flows and support hazard assessment during effusive volcanic crisis.

## 5 Conclusion

Satellite or ground-based remote sensing techniques are key tools to monitor thermal anomalies associated with active lava flows and evaluate their risks on the environment. They rely however, on a not-well-known parameter that controls temperature retrieval, namely spectral emissivity.

This work is an ongoing research that fills the knowledge gap outlined above. Here, we focus on measuring the spectral emissivity at high temperature of natural basaltic compositions and analyzing their chemical, structural, and textural variation before and after IR experiment. Using an IR emission apparatus developed at CEMHTI laboratory, the spectral emissivity up to molten state and wide spectral range (TIR–MIR–SWIR) of homogeneous basaltic glasses is retrieved for the first time. This work shows that spectral emissivity is highly sensible to any change in temperature, wavelength, and primarily depends on sample composition, microstructure, and texture. Results show that the emissivity–temperature relationship for basaltic glass is complex: they are affected by iron clustering, micrometric Fe-Mg-rich crystals crystallization and segregation from the melt towards the surface with increasing temperature. It results in a combined signal between melt and the dominating oxides. The effects of crystals, composition and degree of polymerization on the emissivity–temperature relationship, introduced here for basalts, are crucial to understand the complete thermal evolution of natural lava emissivity, especially in SWIR–MIR ranges where emissivity varies the most. In all compositions investigated, spectral emissivity increases in TIR and decreases in MIR and SWIR with increasing temperature, contrasting with what is commonly found in the literature. We demonstrated that the use of a constant emissivity value for a given rock family without considering these parameters is not a good assumption for temperature retrieval. Finally, we use our laboratory-based emissivity

data to refine Holuhraun lava field temperatures by ~50 K with an improved version of Aufaristama et al., (2018) model.

The ultimate goal of this research is to understand the radiative properties of volcanic molten rocks and hence, better refine temperature measurement from remote sensing radiance data. In turn, it will lead to more accurate lava flow modeling with appropriate rheological information, thus improving hazard assessment in volcanic systems. Despite that measuring spectral emissivity for fully melted magmatic rocks remains difficult to achieve, this work has to be more systematically carry out, as it is crucial for volcanology and geothermal research.

## 6 Acknowledgements

Ida di Carlo and Patricia Benoist (ISTO) are warmly thanked for their support during SEM and EMPA measurements. Gaëlle Prouteau is kindly thanked for providing the MORB sample. Prof. A. Hoskuldsson is thanked for his contribution in fieldwork and sample collection. Prof. B. Scaillet and D. De Sousa Meneses are heartily for their valuable discussions during first version of manuscript. The authors thank the editor Sonia Calvari, Oryaëlle Chevrel and two anonymous reviewers for their excellent, insightful, and constructive comments that greatly improved the focus of this work.

## 7 Authors' contributions

JB: writing, original draft, data collection and analysis, investigation, methodology. AS: supervision, conceptualization, writing, funding acquisition. JA: supervision, conceptualization, writing, funding acquisition. LdC: writing, data analysis, review. LC: data collection, review. HL: review. EV: data collection and analysis, review. CG: data collection and analysis, review. SO: data collection and analysis, review. MA: data application, review.

## 8 Funding

This work is based on JB PhD's thesis at ISTO, Université d'Orléans and was funded by Région Centre and by a grant overseen by the French National Research Agency (ANR) as part of the "Investissements d'Avenir" Programme Equipex PLANEX, ANR-11-EQPX-36, by TelluS Aleas program of CNRS/INSU with RADIABAR project, and Labex Voltaire, ANR-LABX-100-01. The European Volcano Early Warning System (EVE) project grant agreement: 826292 through the Group of Volcanology of Geociencias Barcelona (GEO3BCN-CSIC). TEM: this project has benefited from the facilities of the Plateform MACLE-CVL which was co-funded by the European Union and the Centre-Val de Loire Region (FEDER).

# 9 References


Abtahi, A.A., Kahle, A.B., Abbott, E.A., Gillespie, A.R., Sabol, D., Yamada, G., Pieri, D., 2002. Emissivity Changes in Basalt Cooling After Eruption From PU'U O'O, Kilauea, Hawaii, in: AGU Fall Meeting Abstracts. pp. V71A-1263.

Albert, H., Costa, F., Martí, J., 2015. Timing of Magmatic Processes and Unrest Associated with Mafic Historical Monogenetic Eruptions in Tenerife Island. J. Petrol. 56, 1945–1966. https://doi.org/10.1093/petrology/egv058

Andújar, J., Scaillet, B., 2012. Relationships between pre-eruptive conditions and eruptive styles of phonolite–trachyte magmas. Lithos 152, 122–131. https://doi.org/10.1016/j.lithos.2012.05.009

Applegarth, L.J., Tuffen, H., James, M.R., Pinkerton, H., Cashman, K.V., 2013. Direct observations of degassing-induced crystallization in basalts. Geology 41, 243–246. https://doi.org/10.1130/G33641.1

Aufaristama, M., Hoskuldsson, A., Jonsdottir, I., Ulfarsson, M.O., Thordarson, T., 2018. New Insights for Detecting and Deriving Thermal Properties of Lava Flow Using Infrared Satellite during 2014–2015 Effusive Eruption at Holuhraun, Iceland. Remote Sens. 10, 151. https://doi.org/10.3390/rs10010151

Aufaristama, M., Hoskuldsson, A., Ulfarsson, M., Jonsdottir, I., Thordarson, T., 2019. The 2014–2015 Lava Flow Field at Holuhraun, Iceland: Using Airborne Hyperspectral Remote Sensing for Discriminating the Lava Surface. Remote Sens. 11, 476. https://doi.org/10.3390/rs11050476

Ayache, J., Beaunier, L., Pottu-Boumendil, J., Ehret, G., Laub, D., Mottin, S., 2007. Guide de préparation des échantillons pour la microscopie électronique en transmission. Tome II, Tome II, Intégrations. Publications de l'Université de Saint-Etienne.

Berger, G., Cathala, A., Fabre, S., Borisova, A.Y., Pages, A., Aigouy, T., Esvan, J., Pinet, P., 2019. Experimental exploration of volcanic rock-atmosphere interaction under Venus surface conditions. Icarus 329, 8–23. https://doi.org/10.1016/j.icarus.2019.03.033

Biren, J., Aufaristama, M., Cosson, L., del Carpio, L., Li, H., Andújar, J., Slodczyk, A., 2021. Improving Field Lava Flow Temperatures with Lab-based Spectral Emissivities for The 2014–2015 Holuhraun Eruption. (other). Geology. https://doi.org/10.1002/essoar.10509906.1

Blackett, M., 2017. An Overview of Infrared Remote Sensing of Volcanic Activity. J. Imaging 3, 13. https://doi.org/10.3390/jimaging3020013

Boltzmann, L., 1884. Ableitung des Stefan'schen Gesetzes, betreffend die Abhängigkeit der Wärmestrahlung von der Temperatur aus der electromagnetischen Lichttheorie. Ann. Phys. 258, 291–294. https://doi.org/10.1002/andp.18842580616

Bouhifd, M.A., Whittington, A.G., Withers, A.C., Richet, P., 2013. Heat capacities of hydrous silicate glasses and liquids. Chem. Geol. 346, 125–134. https://doi.org/10.1016/j.chemgeo.2012.10.026

Bouvry, B., Fernández Carrión, A.J., Andújar, J., Veron, E., Ory, S., Brassamin, S., Echegut, P., Escape, C., Nahhas, T., Py, X., Bessada, C., 2017. Mediterranean basin basalts as potential materials for thermal energy storage in concentrated solar plants. Sol. Energy Mater. Sol. Cells 171, 50–59. https://doi.org/10.1016/j.solmat.2017.06.030

Brun, J.-F., 2003. Mesure et analyse de l'émittance spectrale d'oxydes diélectriques à haute température. Une approche des phénomènes préfusionnels. (Physique). Université d'Orléans, Orléans.

Burkhard, D.J.M., 2001. Crystallization and Oxidation of Kilauea Basalt Glass: Processes during Reheating Experiments. J. Petrol. 42, 507–527. https://doi.org/10.1093/petrology/42.3.507

Byrnes, J.M., Ramsey, M.S., King, P.L., Lee, R.J., 2007. Thermal infrared reflectance and emission spectroscopy of quartzofeldspathic glasses. Geophys. Res. Lett. 34. https://doi.org/10.1029/2006GL027893

Cáceres, F., Scheu, B., Hess, K.-U., Cimarelli, C., Vasseur, J., Kaliwoda, M., Dingwell, D.B., 2021. From melt to crystals: The effects of cooling on Fe Ti oxide nanolites crystallisation and melt polymerisation at oxidising conditions. Chem. Geol. 563, 120057. https://doi.org/10.1016/j.chemgeo.2021.120057

Calvari, S., Spampinato, L., Lodato, L., Harris, A.J.L., Patrick, M.R., Dehn, J., Burton, M.R., Andronico, D., 2005. Chronology and complex volcanic processes during the 2002-2003 flank eruption at Stromboli volcano (Italy) reconstructed from direct observations and surveys with a handheld thermal camera. J. Geophys. Res. Solid Earth 110. https://doi.org/10.1029/2004JB003129

Carracedo, J.C., Troll, V., Day, J., Aulinas Junca, M., Soler, V., Deegan, F., Pérez Torrado, F.J., Pinto, G.G., Gazel, E., Rodríguez González, A., Albert Minguez, H., 2022. The 2021 eruption of the Cumbre Vieja Volcanic Ridge on La Palma, Canary Islands (preprint). Physical Sciences and Mathematics. https://doi.org/10.31223/X5D06D

Chen, Y., Zou, C., Mastalerz, M., Hu, S., Gasaway, C., Tao, X., 2015. Applications of Micro-Fourier Transform Infrared Spectroscopy (FTIR) in the Geological Sciences-A Review. Int. J. Mol. Sci. 16, 30223–30250. https://doi.org/10.3390/ijms161226227

Chevrel, M.O., Favalli, M., Villeneuve, N., Harris, A.J.L., Fornaciai, A., Richter, N., Derrien, A., Boissier, P., Di Muro, A., Peltier, A., 2021. Lava flow hazard map of Piton de la Fournaise volcano. Nat. Hazards Earth Syst. Sci. 21, 2355–2377. https://doi.org/10.5194/nhess-21-2355-2021

Chevrel, M.O., Labroquère, J., Harris, A.J.L., Rowland, S.K., 2018. PyFLOWGO: An open-source platform for simulation of channelized lava thermo-rheological properties. Comput. Geosci. 111, 167–180. https://doi.org/10.1016/j.cageo.2017.11.009

Christensen, P.R., Howard, D., Lane, M., Piatek, J., Ruff, S.W., Stefanov, W.L., 2000. A thermal emission spectral library of rock-forming minerals. J. Geophys. Res. 105, 9735–9739. https://doi.org/10.1029/1998JE000624

Colliex, C., Manoubi, T., Ortiz, C., 1991. Electron-energy-loss spectroscopy near-edge fine structures in the iron-oxygen system. Phys. Rev. B 44, 11402–11411. https://doi.org/10.1103/PhysRevB.44.11402

Cook, G.B., Cooper, R.F., Wu, T., 1990. Chemical diffusion and crystalline nucleation during oxidation of ferrous iron-bearing magnesium aluminosilicate glass. J. Non-Cryst. Solids 120, 207–222. https://doi.org/10.1016/0022-3093(90)90205-Z

Cooper, B.L., Salisbury, J.W., Killen, R.M., Potter, A.E., 2002. Midinfrared spectral features of rocks and their powders. J. Geophys. Res. 107, 5017. https://doi.org/10.1029/2000JE001462

Crisp, J., Kahle, A.B., Abbott, E.A., 1990. Thermal infrared spectral character of Hawaiian basaltic glasses. J. Geophys. Res. 95, 21657–21669. https://doi.org/10.1029/JB095iB13p21657

Cullity, B.D., 1978. Elements of x ray diffraction, 2. ed. ed, Addison-Wesley series in metallurgy and materials. Addison-Wesley, Reading, Mass.

De Sousa Meneses, D., Brun, J.-F., Echegut, P., Simon, P., 2004. Contribution of Semi-Quantum Dielectric Function Models to the Analysis of Infrared Spectra. Appl. Spectrosc. 58, 969–974. https://doi.org/10.1366/0003702041655467

De Sousa Meneses, D., Malki, M., Echegut, P., 2006. Optical and structural properties of calcium silicate glasses. J. Non-Cryst. Solids 352, 5301–5308. https://doi.org/10.1016/j.jnoncrysol.2006.08.022

De Sousa Meneses, D., Melin, P., del Campo, L., Cosson, L., Echegut, P., 2015. Apparatus for measuring the emittance of materials from far infrared to visible wavelengths in extreme conditions of temperature. Infrared Phys. Technol. 69, 96–101. https://doi.org/10.1016/j.infrared.2015.01.011

Deer, W.A., Howie, R.A., Zussman, J. (Eds.), 2004. Framework silicates: silica minerals, feldspathoids and the zeolites, 2. ed. ed, Rock-forming minerals. Geological Society, London.

del Campo, L., De Sousa Meneses, D., Blin, A., Rousseau, B., Véron, E., Balat-Pichelin, M., Echegut, P., 2011. High-Temperature Radiative Properties of an Yttria-Stabilized Hafnia Ceramic: High Temperature Radiative Properties of an YSH Ceramic. J. Am. Ceram. Soc. 94, 1859–1864. https://doi.org/10.1111/j.1551-2916.2010.04336.x

del Campo, L., Pérez-Sáez, R.B., Tello, M.J., 2008. Iron oxidation kinetics study by using infrared spectral emissivity measurements below 570°C. Corros. Sci. 50, 194–199. https://doi.org/10.1016/j.corsci.2007.05.029

Di Genova, D., Brooker, R.A., Mader, H.M., Drewitt, J.W.E., Longo, A., Deubener, J., Neuville, D.R., Fanara, S., Shebanova, O., Anzellini, S., Arzilli, F., Bamber, E.C., Hennet, L., La Spina, G.,

Miyajima, N., 2020. In situ observation of nanolite growth in volcanic melt: A driving force for explosive eruptions. Sci. Adv. 6, eabb0413. https://doi.org/10.1126/sciadv.abb0413

Di Genova, D., Caracciolo, A., Kolzenburg, S., 2018. Measuring the degree of "nanotilization" of volcanic glasses: Understanding syn-eruptive processes recorded in melt inclusions. Lithos 318–319, 209–218. https://doi.org/10.1016/j.lithos.2018.08.011

Di Genova, D., Kolzenburg, S., Vona, A., Chevrel, M.O., Hess, K.-U., Neuville, D.R., Ertel-Ingrisch, W., Romano, C., Dingwell, D.B., 2016. Raman spectra of Martian glass analogues: A tool to approximate their chemical composition: Raman Spectra of Martian Glass Analogues. J. Geophys. Res. Planets 121, 740–752. https://doi.org/10.1002/2016JE005010

Di Genova, D., Vasseur, J., Hess, K.-U., Neuville, D.R., Dingwell, D.B., 2017. Effect of oxygen fugacity on the glass transition, viscosity and structure of silica- and iron-rich magmatic melts. J. Non-Cryst. Solids 470, 78–85. https://doi.org/10.1016/j.jnoncrysol.2017.05.013

D'Ippolito, V., Andreozzi, G.B., Bersani, D., Lottici, P.P., 2015. Raman fingerprint of chromate, aluminate and ferrite spinels. J. Raman Spectrosc. 46, 1255–1264. https://doi.org/10.1002/jrs.4764

Donaldson Hanna, K.L., Thomas, I.R., Bowles, N.E., Greenhagen, B.T., Pieters, C.M., Mustard, J.F., Jackson, C.R.M., Wyatt, M.B., 2012. Laboratory emissivity measurements of the plagioclase solid solution series under varying environmental conditions. J. Geophys. Res. Planets 117, n/a-n/a. https://doi.org/10.1029/2012JE004184

Eckes, M., Gibert, B., De Sousa Meneses, D., Malki, M., Echegut, P., 2013. High-temperature infrared properties of forsterite. Phys. Chem. Miner. 40, 287–298. https://doi.org/10.1007/s00269-013-0570-z

Ferrari, S., Nestola, F., Massironi, M., Maturilli, A., Helbert, J., Alvaro, M., Domeneghetti, M.C., Zorzi, F., 2014. In-situ high-temperature emissivity spectra and thermal expansion of C2/c pyroxenes: Implications for the surface of Mercury. Am. Mineral. 99, 786–792. https://doi.org/10.2138/am.2014.4698

Fornaciai, A., Andronico, D., Favalli, M., Scampinato, L., Branca, S., Lodato, L., Bonforte, A., Nannipieri, L., 2021. The 2004–2005 Mt. Etna Compound Lava Flow Field: A Retrospective Analysis by Combining Remote and Field Methods. J. Geophys. Res. Solid Earth 126. https://doi.org/10.1029/2020JB020492

Geiger, H., Mattsson, T., Deegan, F.M., Troll, V.R., Burchardt, S., Gudmundsson, Ó., Tryggvason, A., Krumbholz, M., Harris, C., 2016. Magma plumbing for the 2014-2015 Holuhraun eruption, Iceland: Magma Plumbing for Holuhraun. Geochem. Geophys. Geosystems 17, 2953–2968. https://doi.org/10.1002/2016GC006317

Gillespie, A., Rokugawa, S., Matsunaga, T., Cothern, J.S., Hook, S., Kahle, A.B., 1998. A temperature and emissivity separation algorithm for Advanced Spaceborne Thermal Emission and Reflection Radiometer (ASTER) images. IEEE Trans. Geosci. Remote Sens. 36, 1113–1126. https://doi.org/10.1109/36.700995

Giordano, D., Nichols, A.R.L., Dingwell, D.B., 2005. Glass transition temperatures of natural hydrous melts: a relationship with shear viscosity and implications for the welding process. J. Volcanol. Geotherm. Res. 142, 105–118. https://doi.org/10.1016/j.jvolgeores.2004.10.015

Giordano, D., Polacci, M., Longo, A., Papale, P., Dingwell, D.B., Boschi, E., Kasereka, M., 2007. Thermo-rheological magma control on the impact of highly fluid lava flows at Mt. Nyiragongo. Geophys. Res. Lett. 34, L06301. https://doi.org/10.1029/2006GL028459

Giordano, D., Vona, A., Gonzalez-Garcia, D., Allabar, A., Kolzenburg, S., Polo, L.A., de Assis Janasi, V., Behrens, H., De Campos, C.P., De Cristofaro, S., Freitas Guimarães, L., Nowak, M., Müller, D., Günther, A., Masotta, M., Roverato, M., Romano, C., Dingwell, D.B., 2021. Viscosity of Palmas-type magmas of the Paraná Magmatic Province (Rio Grande do Sul State, Brazil): Implications for high-temperature silicic volcanism. Chem. Geol. 560, 119981. https://doi.org/10.1016/j.chemgeo.2020.119981

Giuliani, L., Iezzi, G., Hippeli, T., Davis, M., Elbrecht, A., Vetere, F., Nazzari, M., Mollo, S., 2020. The Onset and Solidification Path of a Basaltic Melt by in situ Differential Scanning Calorimetry (DSC) and ex situ Investigations. Front. Earth Sci. 8, 337. https://doi.org/10.3389/feart.2020.00337

Golla-Schindler, U., Benner, G., Putnis, A., 2003. Laterally resolved EELS for ELNES mapping of the Fe L2,3- and O K-edge. Ultramicroscopy 96, 573–582. https://doi.org/10.1016/S0304-3991(03)00118-9

Golla-Schindler, U., Hinrichs, R., Bomati-Miguel, O., Putnis, A., 2006. Determination of the oxidation state for iron oxide minerals by energy-filtering TEM. Micron 37, 473–477. https://doi.org/10.1016/j.micron.2005.11.002

González-García, D., Giordano, D., Allabar, A., Andrade, F.R.D., Polo, L.A., Janasi, V.A., Lucchetti, A.C.F., Hess, K.-U., De Campos, C.P., Dingwell, D.B., 2021. Retrieving dissolved H2O content from micro-Raman spectroscopy on nanolitized silicic glasses: Application to volcanic products of the Paraná Magmatic Province, Brazil. Chem. Geol. 567, 120058. https://doi.org/10.1016/j.chemgeo.2021.120058

Halldórsson, S.A., Bali, E., Hartley, M.E., Neave, D.A., Peate, D.W., Guðfinnsson, G.H., Bindeman, I., Whitehouse, M.J., Riishuus, M.S., Pedersen, G.B.M., Jakobsson, S., Askew, R., Gallagher, C.R., Guðmundsdóttir, E.R., Gudnason, J., Moreland, W.M., Óskarsson, B.V., Nikkola, P., Reynolds, H.I., Schmith, J., Thordarson, T., 2018. Petrology and geochemistry of the 2014–2015 Holuhraun eruption, central Iceland: compositional and mineralogical characteristics, temporal variability and magma storage. Contrib. Mineral. Petrol. 173, 64. https://doi.org/10.1007/s00410-018-1487-9

Hamilton, V.E., 2010. Thermal infrared (vibrational) spectroscopy of Mg–Fe olivines: A review and applications to determining the composition of planetary surfaces. Geochemistry 70, 7–33. https://doi.org/10.1016/j.chemer.2009.12.005

Hamilton, V.E., 2000. Thermal infrared emission spectroscopy of the pyroxene mineral series. J. Geophys. Res. Planets 105, 9701–9716. https://doi.org/10.1029/1999JE001112

Harris, A., 2013. Thermal remote sensing of active volcanoes: a user's manual. Cambridge Univ. Press, Cambridge.

Harris, A.J.L., De Groeve, T., Garel, F., Carn, S.A., 2016. Detecting, modelling and responding to effusive eruptions, Special Publications. Geological Society of London.

Harris, A.J.L., Thornber, C.R., 1999. Complex effusive events at Kīlauea as documented by the GOES satellite and remote video cameras. Bull. Volcanol. 61, 382–395. https://doi.org/10.1007/s004450050289

Howell, J.R., Menguc, M.P., Siegel, R., 2015. Thermal Radiation Heat Transfer, 6th ed. CRC Press.

Huang, E., Chen, C.H., Huang, T., Lin, E.H., Xu, J., 2000. Raman spectroscopic characteristics of Mg-Fe-Ca pyroxenes. Am. Mineral. 85, 473–479. https://doi.org/10.2138/am-2000-0408

Jiménez-Mejías, M., Andújar, J., Scaillet, B., Casillas, R., 2021. Experimental determination of H2O and CO2 solubilities of mafic alkaline magmas from Canary Islands. Comptes Rendus Géoscience 353, 1–26. https://doi.org/10.5802/crgeos.84

Kaneko, T., Yasuda, A., Fujii, T., 2021. Simple empirical method for estimating lava-effusion rate using nighttime Himawari-8 1.6-μm infrared images. Earth Planets Space 73, 37. https://doi.org/10.1186/s40623-021-01372-w

King, P.L., McMillan, P.F., Moore, G.M., 2004. Chapter 4. Infrared spectroscopy of silicate glasses with application to natural systems. p. 42.

Kolzenburg, S., Giordano, D., Cimarelli, C., Dingwell, D.B., 2016. In situ thermal characterization of cooling/crystallizing lavas during rheology measurements and implications for lava flow emplacement. Geochim. Cosmochim. Acta 195, 244–258. https://doi.org/10.1016/j.gca.2016.09.022

Kolzenburg, S., Giordano, D., Giordano, D., Di Muro, A., Di Muro, A., Dingwell, D., Dingwell, D., 2018. Equilibrium Viscosity and Disequilibrium Rheology of a high Magnesium Basalt from Piton De La Fournaise volcano, La Reunion, Indian Ocean, France. Ann. Geophys. 61, 4. https://doi.org/10.4401/ag-7839

Kolzenburg, S., Giordano, D., Thordarson, T., Höskuldsson, A., Dingwell, D.B., 2017. The rheological evolution of the 2014/2015 eruption at Holuhraun, central Iceland. Bull. Volcanol. 79, 45. https://doi.org/10.1007/s00445-017-1128-6

Lalla, E.A., Lopez-Reyes, G., Sansano, A., Sanz-Arranz, A., Martínez-Frías, J., Medina, J., Rull-Pérez, F., 2016. Raman-IR vibrational and XRD characterization of ancient and modern

mineralogy from volcanic eruption in Tenerife Island: Implication for Mars. Geosci. Front. 7, 673–681. https://doi.org/10.1016/j.gsf.2015.07.009

Lee, R.J., King, P.L., Ramsey, M.S., 2010. Spectral analysis of synthetic quartzofeldspathic glasses using laboratory thermal infrared spectroscopy. J. Geophys. Res. 115, 9. https://doi.org/10.1029/2009JB006672

Lee, R.J., Ramsey, M.S., King, P.L., 2013. Development of a new laboratory technique for high-temperature thermal emission spectroscopy of silicate melts. J. Geophys. Res. Solid Earth 118, 1968–1983. https://doi.org/10.1002/jgrb.50197

Li, H., Andujar, J., Slodczyk, A., De Sousa Meneses, D., Scaillet, B., Echegut, P., Biren, J., Oppenheimer, C., 2021. Spectral Emissivity of Phonolite Lava at High Temperature. IEEE Trans. Geosci. Remote Sens. 1–15. https://doi.org/10.1109/TGRS.2021.3104657

Lombardo, V., Buongiorno, M.F., 2006. Lava flow thermal analysis using three infrared bands of remote-sensing imagery: A study case from Mount Etna 2001 eruption. Remote Sens. Environ. 101, 141–149. https://doi.org/10.1016/j.rse.2005.12.008

Lombardo, V., Pick, L., Spinetti, C., Tadeucci, J., Zakšek, K., 2020. Temperature and Emissivity Separation 'Draping' Algorithm Applied to Hyperspectral Infrared Data. Remote Sens. 12, 2046. https://doi.org/10.3390/rs12122046

Manylov, M.S., Gutnikov, S.I., Pokholok, K.V., Lazoryak, B.I., Lipatov, Y.V., 2013. Crystallization mechanism of basalt glass fibers in air. Mendeleev Commun. 23, 361–363. https://doi.org/10.1016/j.mencom.2013.11.021

Morimoto, N., 1988. Nomenclature of pyroxenes. Bull. Mineralogie 111, 535–550. https://doi.org/10.3406/bulmi.1988.8099

Mottl, M.J., Davis, E.E., Fisher, A.T., Slack, J.F. (Eds.), 1994. Proceedings of the Ocean Drilling Program, 139 Scientific Results, Proceedings of the Ocean Drilling Program. Ocean Drilling Program. https://doi.org/10.2973/odp.proc.sr.139.1994

Mujin, M., Nakamura, M., Matsumoto, M., 2021. In-situ FE-SEM observation of the growth behaviors of Fe particles at magmatic temperatures. J. Cryst. Growth 560–561, 126043. https://doi.org/10.1016/j.jcrysgro.2021.126043

Nádudvari, Á., Abramowicz, A., Maniscalco, R., Viccaro, M., 2020. The Estimation of Lava Flow Temperatures Using Landsat Night-Time Images: Case Studies from Eruptions of Mt. Etna and Stromboli (Sicily, Italy), Kilauea (Hawaii Island), and Eyjafjallajökull and Holuhraun (Iceland). Remote Sens. 12, 2537. https://doi.org/10.3390/rs12162537

Neal, C.A., Brantley, S.R., Antolik, L., Babb, J.L., Burgess, M., Calles, K., Cappos, M., Chang, J.C., Conway, S., Desmither, L., Dotray, P., Elias, T., Fukunaga, P., Fuke, S., Johanson, I.A., Kamibayashi, K., Kauahikaua, J., Lee, R.L., Pekalib, S., Miklius, A., Million, W., Moniz, C.J., Nadeau, P.A., Okubo, P., Parcheta, C., Patrick, M.R., Shiro, B., Swanson, D.A., Tollett, W., Trusdell, F., Younger, E.F., Zoeller, M.H., Montgomery-Brown, E.K., Anderson, K.R., Poland, M.P., Ball, J.L., Bard, J., Coombs, M., Dietterich, H.R., Kern, C., Thelen, W.A., Cervelli, P.F., Orr, T., Houghton, B.F., Gansecki, C., Hazlett, R., Lundgren, P., Diefenbach, A.K., Lerner, A.H., Waite, G., Kelly, P., Clor, L., Werner, C., Mulliken, K., Fisher, G., Damby, D., 2019. The 2018 rift eruption and summit collapse of Kīlauea Volcano. Science 363, 367–374. https://doi.org/10.1126/science.aav7046

Neave, D.A., Bali, E., Guðfinnsson, G.H., Halldórsson, S.A., Kahl, M., Schmidt, A.-S., Holtz, F., 2019. Clinopyroxene–Liquid Equilibria and Geothermobarometry in Natural and Experimental Tholeiites: the 2014–2015 Holuhraun Eruption, Iceland. J. Petrol. 60, 1653–1680. https://doi.org/10.1093/petrology/egz042

Oppenheimer, C., 1993. Thermal distributions of hot volcanic surfaces constrained using three infrared bands of remote sensing data. Geophys. Res. Lett. 20, 431–434. https://doi.org/10.1029/93GL00500

Pedersen, G.B.M., Höskuldsson, A., Dürig, T., Thordarson, T., Jónsdóttir, I., Riishuus, M.S., Óskarsson, B.V., Dumont, S., Magnusson, E., Gudmundsson, M.T., Sigmundsson, F., Drouin, V.J.P.B., Gallagher, C., Askew, R., Gudnason, J., Moreland, W.M., Nikkola, P., Reynolds, H.I., Schmith, J., 2017. Lava field evolution and emplacement dynamics of the 2014–2015 basaltic fissure eruption at Holuhraun, Iceland. J. Volcanol. Geotherm. Res. 340, 155–169. https://doi.org/10.1016/j.jvolgeores.2017.02.027

Pisello, A., Vetere, F.P., Bisolfati, M., Maturilli, A., Morgavi, D., Pauselli, C., Iezzi, G., Lustrino, M., Perugini, D., 2019. Retrieving magma composition from TIR spectra: implications for terrestrial planets investigations. Sci. Rep. 9, 15200. https://doi.org/10.1038/s41598-019-51543-9

Plank, S., Marchese, F., Filizzola, C., Pergola, N., Neri, M., Nolde, M., Martinis, S., 2019. The July/August 2019 Lava Flows at the Sciara del Fuoco, Stromboli–Analysis from Multi-Sensor Infrared Satellite Imagery. Remote Sens. 11, 2879. https://doi.org/10.3390/rs11232879

Prouteau, G., Scaillet, B., Pichavant, M., Maury, R., 2001. Evidence for mantle metasomatism by hydrous silicic melts derived from subducted oceanic crust. Nature 410, 197–200. https://doi.org/10.1038/35065583

Ramírez-González, L.M., Aufaristama, M., Jónsdóttir, I., Höskuldsson, Á., þórðarson, þorvaldur, Proietti, N.M., Kraft, G., McQuilkin, J., 2019. Remote sensing of surface Hydrothermal Alteration, identification of Minerals and Thermal anomalies at Sveifluháls-Krýsuvík high-temperature Geothermal field, SW Iceland. IOP Conf. Ser. Earth Environ. Sci. 254, 13. https://doi.org/10.1088/1755-1315/254/1/012005

Ramsey, M., Chevrel, M.O., Coppola, D., Harris, A.J.L., 2019. The influence of emissivity on the thermo-rheological modeling of the channelized lava flows at Tolbachik volcano. Ann. Geophys. 62, 24. https://doi.org/10.4401/ag-8077

Ramsey, M.S., Christensen, P.R., 1998. Mineral abundance determination: Quantitative deconvolution of thermal emission spectra. J. Geophys. Res. Solid Earth 103, 577–596. https://doi.org/10.1029/97JB02784

Ramsey, M.S., Harris, A.J.L., Crown, D.A., 2016. What can thermal infrared remote sensing of terrestrial volcanoes tell us about processes past and present on Mars? J. Volcanol. Geotherm. Res. 311, 198–216. https://doi.org/10.1016/j.jvolgeores.2016.01.012

Robert, G., Whittington, A.G., Stechern, A., Behrens, H., 2014. Heat capacity of hydrous basaltic glasses and liquids. J. Non-Cryst. Solids 389, 19–30. https://doi.org/10.1016/j.jnoncrysol.2014.02.011

Rogic, N., Cappello, A., Ferrucci, F., 2019a. Role of Emissivity in Lava Flow 'Distance-to-Run' Estimates from Satellite-Based Volcano Monitoring. Remote Sens. 11, 662. https://doi.org/10.3390/rs11060662

Rogic, N., Cappello, A., Ganci, G., Maturilli, A., Rymer, H., Blake, S., Ferrucci, F., 2019b. Spaceborne EO and a Combination of Inverse and Forward Modelling for Monitoring Lava Flow Advance. Remote Sens. 11, 3032. https://doi.org/10.3390/rs11243032

Rozenbaum, O., De Sousa Meneses, D., Echegut, P., 2009. Texture and Porosity Effects on the Thermal Radiative Behavior of Alumina Ceramics. Int. J. Thermophys. 30, 580–590. https://doi.org/10.1007/s10765-008-0510-1

Rozenbaum, O., Meneses, D.D.S., Auger, Y., Chermanne, S., Echegut, P., 1999. A spectroscopic method to measure the spectral emissivity of semi-transparent materials up to high temperature. Rev. Sci. Instrum. 70, 4020–4025. https://doi.org/10.1063/1.1150028

Ruff, S.W., Christensen, P.R., Barbera, P.W., Anderson, D.L., 1997. Quantitative thermal emission spectroscopy of minerals: A laboratory technique for measurement and calibration. J. Geophys. Res. Solid Earth 102, 14899–14913. https://doi.org/10.1029/97JB00593

Stefan, J., 1879. Über die Beziehung zwischen der Wärmestrahlung und der Temperatur. Sitzungsberichte Math.-Naturwissenschaftlichen Cl. Kais. Akad. Wiss. 391–428.

Takeuchi, S., 2011. Preeruptive magma viscosity: An important measure of magma eruptibility. J. Geophys. Res. 116, B10201. https://doi.org/10.1029/2011JB008243

Thompson, J.O., Ramsey, M.S., 2021. The influence of variable emissivity on lava flow propagation modeling. Bull. Volcanol. 83, 41. https://doi.org/10.1007/s00445-021-01462-3

Thompson, J.O., Ramsey, M.S., 2020. Spatiotemporal variability of active lava surface radiative properties using ground-based multispectral thermal infrared data. J. Volcanol. Geotherm. Res. 408, 107077. https://doi.org/10.1016/j.jvolgeores.2020.107077

Thompson, J.O., Williams, D.B., Lee, R.J., Ramsey, M.S., 2021. Quantitative Thermal Emission Spectroscopy at High Temperatures: A Laboratory Approach for Measurement and Calibration. J. Geophys. Res. Solid Earth 126. https://doi.org/10.1029/2021JB022157

Thomson, J.L., Salisbury, J.W., 1993. The mid-infrared reflectance of mineral mixtures (7–14 μm). Remote Sens. Environ. 45, 1–13. https://doi.org/10.1016/0034-4257(93)90077-B

Yang, J., Duan, S.-B., Zhang, X., Wu, P., Huang, C., Leng, P., Gao, M., 2020. Evaluation of Seven Atmospheric Profiles from Reanalysis and Satellite-Derived Products: Implication for Single-Channel Land Surface Temperature Retrieval. Remote Sens. 12, 791. https://doi.org/10.3390/rs12050791

Zakšek, K., Shirzaei, M., Hort, M., 2013. Constraining the uncertainties of volcano thermal anomaly monitoring using a Kalman filter technique. Geol. Soc. Lond. Spec. Publ. 380, 137–160. https://doi.org/10.1144/SP380.5

Zinin, P., Tatsumi-Petrochilos, L., Bonal, L., Acosta, T., Hammer, J., Gilder, S., Fuller, M., 2011. Raman spectroscopy of titanomagnetites: Calibration of the intensity of Raman peaks as a sensitive indicator for their Ti content. Am. Mineral. 96, 1537–1546. https://doi.org/10.2138/am.2011.3745

*Table 1: Review of spectral emissivity measurements at relevant magmatic conditions.*

| ***Sample*** | ***Preparation*** | ***$T_{max}$ (K)*** | ***Wavelength (µm)*** | ***Instrument*** | ***ε-T behavior*** | ***Reference*** |
|---|---|---|---|---|---|---|
| *Pu'u 'Ō'ō (Hawaii) basalt* | *no mention* | *1323* | *1.25-15* | *hemispheric reflector and field* | *ε decreases with T in TIR* | *Abtahi et al. 2002* |
| *Rhyolite* | *synthetic glass powder, 20-80 µm* | *1773* | *6-15* | *FTIR Nicolet Nexus 670* | *ε decreases with T in TIR* | *Lee et al. 2013* |
| *alkaline + subalkaline series* | *synthesized glasses, powder <25 µm* | *873* | *7-14* | *FTIR Brucker Vertex 80v* | *ε decreases with T in TIR* | *Pisello et al. 2019* |
| *Basalt (Etna)* | *powder, 1000–3000 µm* | *900* | *5-15* | *FTIR MIDAC M2000, Brucker Vertex 80v* | *ε decreases with T in TIR* | *Rogic et al. 2019, 2019b* |
| *Basalt (Kilauea)* | *powder, 100–350 µm* | *1573* | *2.5-20* | *FTIR Nicolet Nexus 670* | *ε decreases with T in TIR, MIR* | *Thompson and Ramsey 2021* |
| *Basalt (Etna)* | *powder, 100–350 µm* | *1373* | *2.17-21* | *Nicolet Nexus 870 FTIR* | *ε decreases with T in TIR, MIR, SWIR* | *Rogic et al. 2022* |
| *Basalt (Etna)* | *granulate* | *1573* | *1.5-2.5* | *Spectroradiometer ASD FieldSpec Pro* | *No significant variation of ε (>0.9) in SWIR* | *Lombardo et al. 2020* |
| *Phonolites (El Teide, Erebus)* | *polished glasses, 1.5 mm thick* | *1600* | *1-25* | *FTIR Brucker Vertex 80v et 70* | *ε increases with T in TIR, variable in MIR, SWIR* | *Li et al. 2021* |
| *7 Mediterranean Basalts* | *polished, 3.0 mm thick* | *1273* | *1-25* | *FTIR Brucker Vertex 80v et 70* | *ε increases with T in TIR, constant in MIR, SWIR* | *Bouvry et al. 2017* |
| *Mg-O rich carbonatite and ijolite* | *powder, 63-250 µm* | *1000* | *1-16* | *FTIR Brucker Vertex 80v* | *ε increases with T in TIR for Ijolite and ε constant for carbonatite* | *Mueller et al. 2013* |

*Table 2: Chemical composition (EMPA) before and after IR experiments for the studied samples: B-glass, B-Nat, MORB, and Fasnia.*

| Oxide wt. % | B-glass BeforeIR | | B-glass AfterIR | | B-Nat-AfterIR | | MORB-BeforeIR | | MORB-AfterIR | | FASNIA-BeforeIR | | FASNIA-AfterIR | |
|---|---|---|---|---|---|---|---|---|---|---|---|---|---|---|
| | Glass | S.D. | Glass | S.D. | Glass | S.D. | Glass | S.D. | Glass | S.D. | Glass | S.D. | Glass | S.D. |
| # analysis | 34 | - | 79 | - | 19 | - | 25 | - | 35 | - | 15 | - | 15 | - |
| **$SiO_2$** | 48.91 | 0.58 | 50.19 | 2.01 | 51.65 | 1.87 | 49.65 | 0.69 | 50.83 | 1.15 | 44.19 | 0.32 | 47.40 | 0.53 |
| **$TiO_2$** | 2.01 | 0.19 | 1.87 | 0.13 | 1.98 | 0.24 | 2.45 | 0.14 | 2.26 | 0.23 | 3.71 | 0.14 | 3.92 | 0.15 |
| **$Al_2O_3$** | 13.58 | 0.38 | 13.71 | 0.33 | 13.10 | 0.39 | 13.71 | 0.28 | 13.25 | 0.68 | 15.10 | 0.22 | 15.44 | 0.66 |
| **FeO tot** | 13.69 | 0.87 | 12.64 | 1.07 | 11.32 | 1.30 | 13.01 | 0.31 | 11.66 | 1.63 | 12.44 | 0.34 | 8.72 | 0.47 |
| **MnO** | 0.24 | 0.09 | 0.20 | 0.07 | 0.25 | 0.10 | 0.20 | 0.06 | 0.22 | 0.08 | 0.19 | 0.07 | 0.14 | 0.08 |
| **MgO** | 6.95 | 0.36 | 6.95 | 0.34 | 7.01 | 0.45 | 6.57 | 0.07 | 6.29 | 0.41 | 7.85 | 0.09 | 6.71 | 0.33 |
| **CaO** | 11.85 | 0.29 | 11.62 | 0.45 | 11.82 | 0.79 | 10.97 | 0.10 | 11.24 | 0.75 | 10.42 | 0.07 | 11.56 | 0.36 |
| **$Na_2O$** | 2.50 | 0.09 | 2.42 | 0.21 | 2.43 | 0.32 | 2.78 | 0.09 | 2.82 | 0.23 | 3.62 | 0.10 | 3.69 | 0.15 |
| **$K_2O$** | 0.23 | 0.04 | 0.21 | 0.04 | 0.23 | 0.07 | 0.26 | 0.06 | 0.26 | 0.06 | 1.61 | 0.10 | 1.46 | 0.11 |
| **$Cr_2O_3$** | 0.01 | 0.01 | 0.01 | 0.02 | 0.01 | 0.02 | 0.01 | 0.02 | 0.09 | 0.14 | 0.04 | 0.03 | 0.01 | 0.02 |
| **$P_2O_5$** | - | - | - | - | 0.22 | 0.09 | 0.40 | 0.23 | 0.36 | 0.32 | 0.84 | 0.12 | 0.91 | 0.18 |
| **NiO** | 0.02 | 0.04 | 0.09 | 0.09 | - | - | - | - | - | - | - | - | 0.04 | 0.08 |
| **Total %** | 100.00 | - | 100.00 | - | 100.00 | - | 100.00 | - | 100.00 | - | 100.00 | - | 100.00 | - |

*Table 3: Interpretation of the physical processes for Bárðarbunga glass observed with temperature increase in agreement with DSC, XRD, and Raman analyses.*

| **Temperature (K)** | **Main IR Spectral Features** | **Physical Process** |
|---|---|---|
| <1020 | Wide Reststrahlen band and CF in TIR, | Radiative response of semi-transparent homogeneous glass |
| | ε≥0.9 in MIR but presence of TF | |
| 1020-1150 | jump-like increase of ε ≥0.95 in MIR/SWIR | Opacification due to the formation of Fe-Mg-rich clusters |
| 1150-1350 | New thin absorption bands in TIR, | Crystallization of Fe-Mg-rich oxides in the melting glass |
| | Wide bands in MIR, SWIR | |
| 1350-1550 | Overall ε decrease, loss of CF | Phase segregation: melt + Fe-rich oxides layer in surface<br>Radiative response of Fe-rich oxides layer exclusively |
| >1550 | Wide Reststrahlen bands in TIR, | Radiative response of homogeneous melt |

Figures

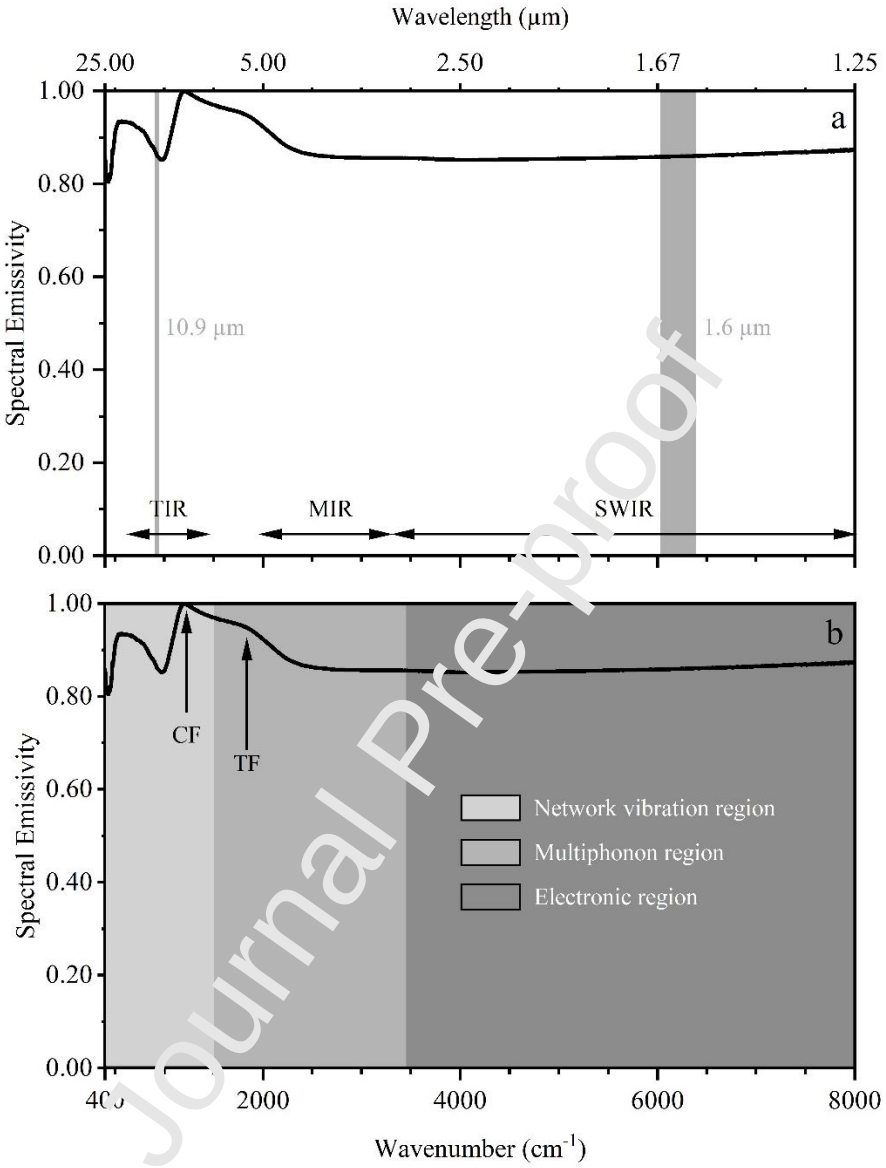


*Figure 1: Example of emissivity spectrum of melted Bárðarbunga sample (recorded at 1787 K, 3 mm thickness) with clearly marked: a) characteristic spectral ranges: TIR, MIR, SWIR and bands 1.6 μm and 10.9 μm commonly used in Remote Sensing applications. Note that the bands at 1.6 and 10.9 μm are further used to refine Holuhraun lava flow temperature; b) Physical spectral regions of interest: network vibration, multiphonon and electronic regions together with spectral features such as CF: Christiansen Feature, and TF: Transmissivity Front.*

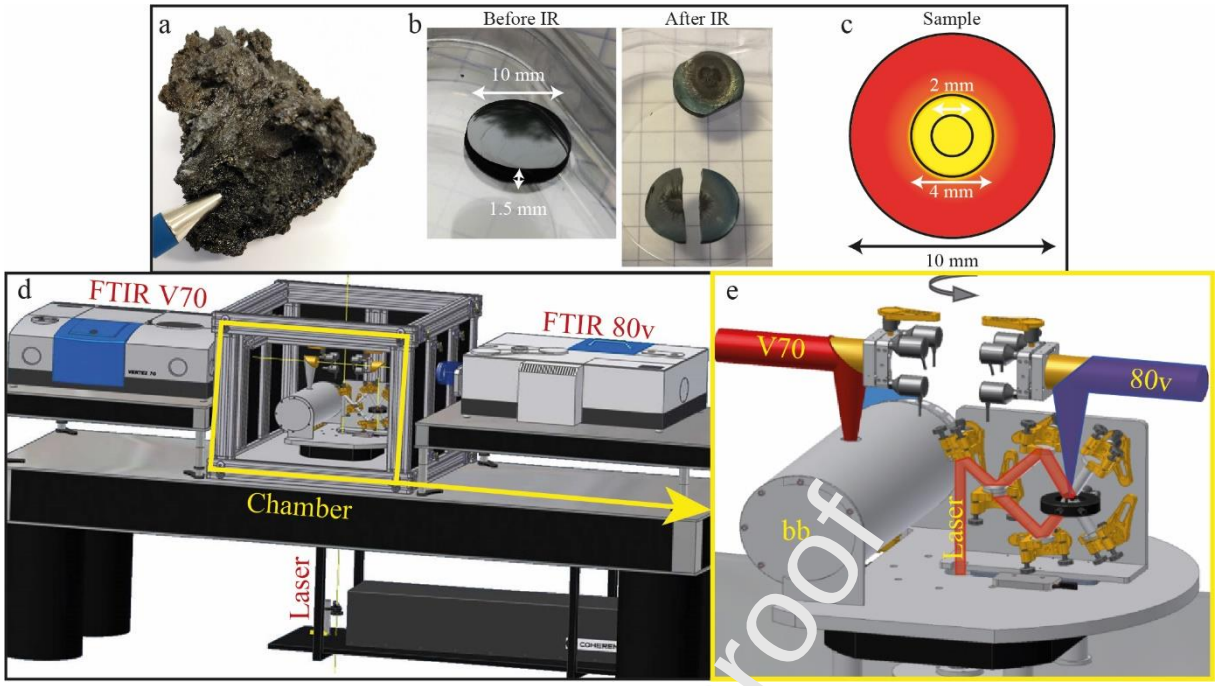


*Figure 2: a) Scoriae of lapilli size from the 2014–2015 Holuhraun eruption used as starting material. b) Pictures of the polished glass samples before and after IR experiment. c) Schematic view of the 10 mm diameter sample with the 2 mm measuring area within the 4 mm homogeneous heating area. d) Schematic of the IR emission apparatus (De Sousa Meneses et al. 2015). e) Schematic of the apparatus chamber interior: bb as the blackbody reference; V70 and 80v optical paths from the sample to the respective FTIR spectrometers; the sample holder on a 180° rotary turntable; the $CO_2$ laser as the heating source (schematics d,e, courtesy of Philippe Melin).*

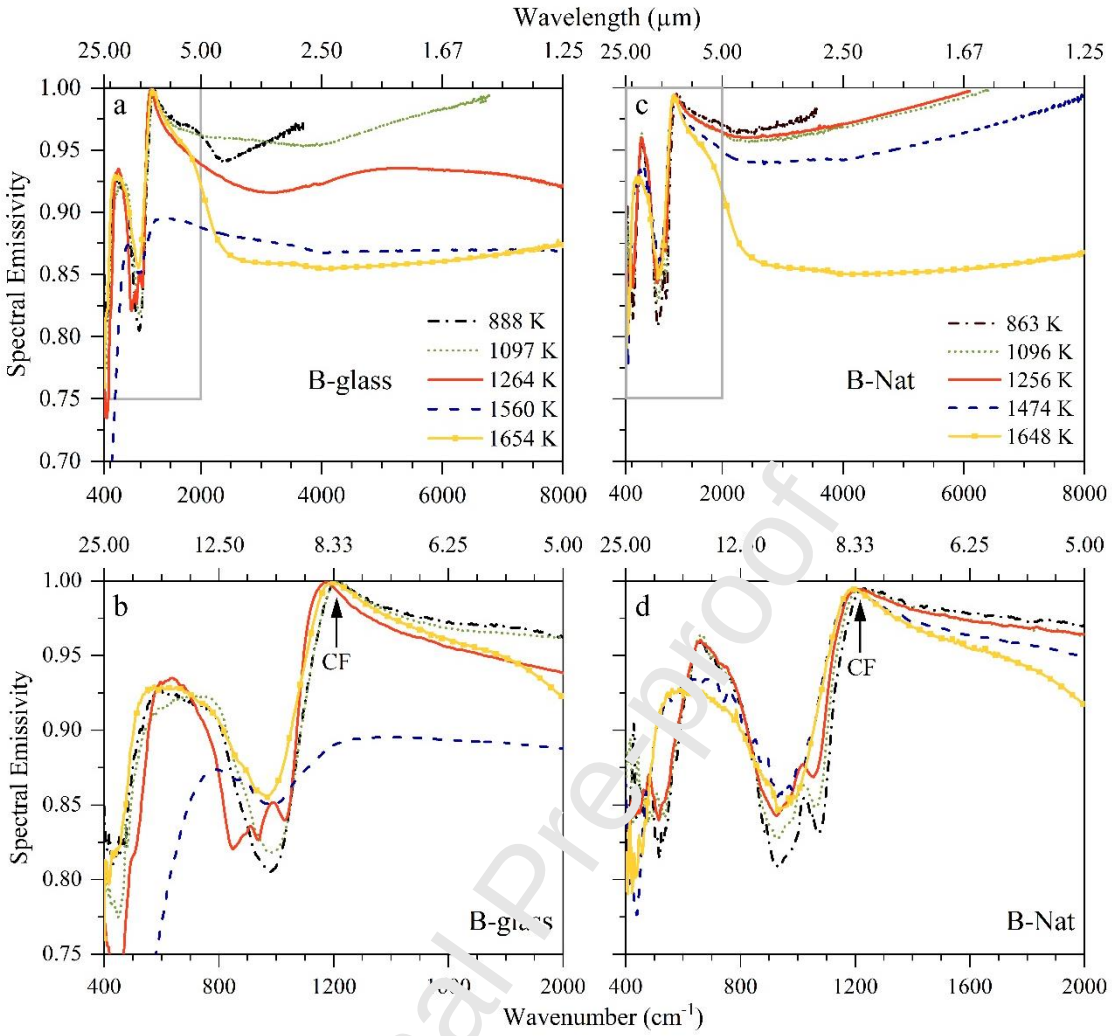


Figure 3: Spectral emissivity evolution with temperature and wavenumber for a,b) Bárðarbunga glass, and c,d) Bárðarbunga Natural (thickness: 1.5 mm, and 3.0 mm at ~1650 K). b), d) Zoom on TIR range (8–12 μm). Note the limited spectral range for the spectra recorded at lower temperature because of the insufficient radiation achieving detector. CF: Christiansen Feature.

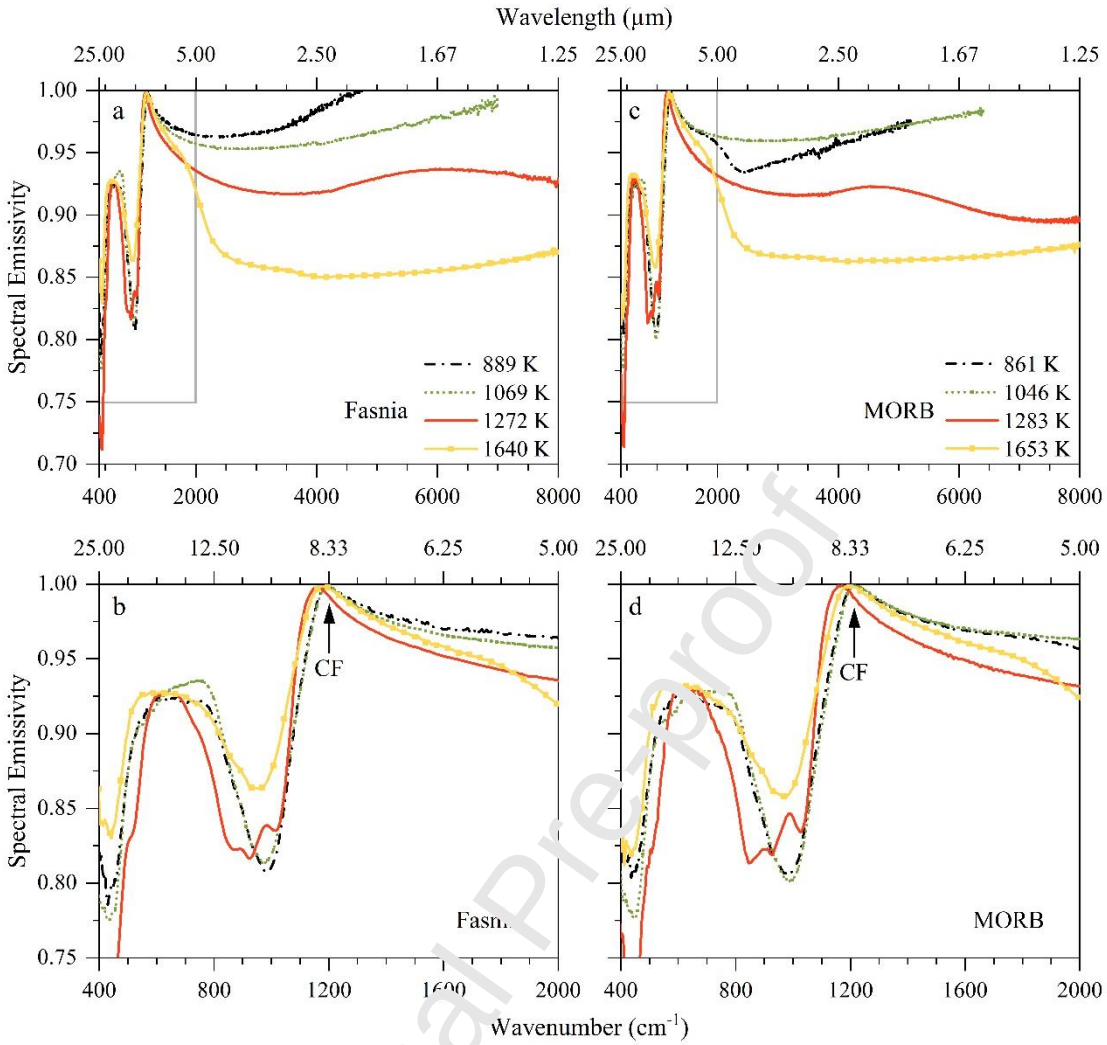


*Figure 4: Spectral emissivity evolution with temperature and wavenumber for a,b) Fasnia and c,d) MORB (thickness: 1.5 mm, and 3.0 mm at ~1650 K). b), d) Zoom of TIR spectral range (8–12 µm). Note the limited spectral range for the spectra recorded at lower temperature because of the insufficient radiation achieving detector. CF: Christiansen Feature.*

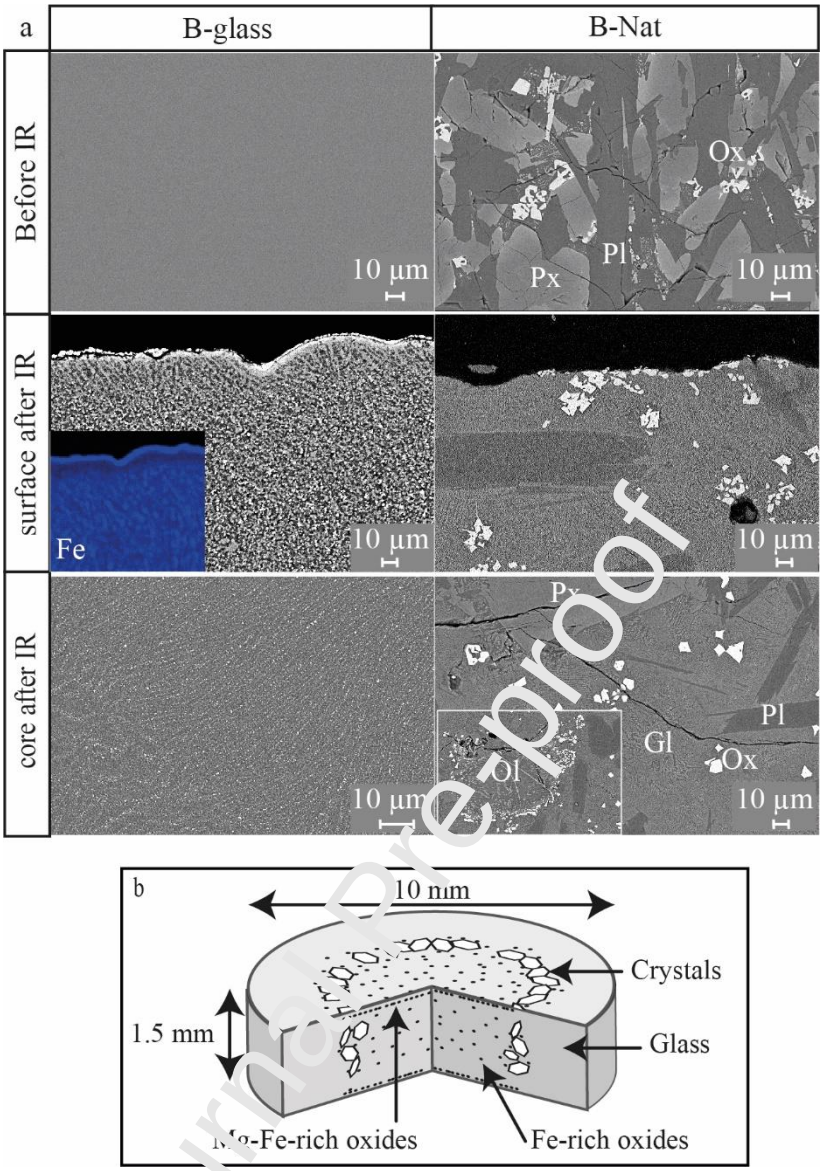


*Figure 5: a) SEM pictures of Bárðarbunga glass (B-glass) and Bárðarbunga Natural (B-Nat) before IR (above) and after IR measurements (below); the surface and the core are distingushed after IR. B-glass shows a distinct iron-rich oxide layer at the surface (insert: Fe chemical map obtained with EMPA). Insert in bottom right; remnant olivine mostly transformed into Fe-rich oxides. Ox-oxide, Pl-plagioclase, Px-pyroxene, Ol-olivine, Gl-glass. b) Interpretation sketch of forming Fe-Mg-rich oxide layer formation at T >1150 K during IR experiment (not on scale).*

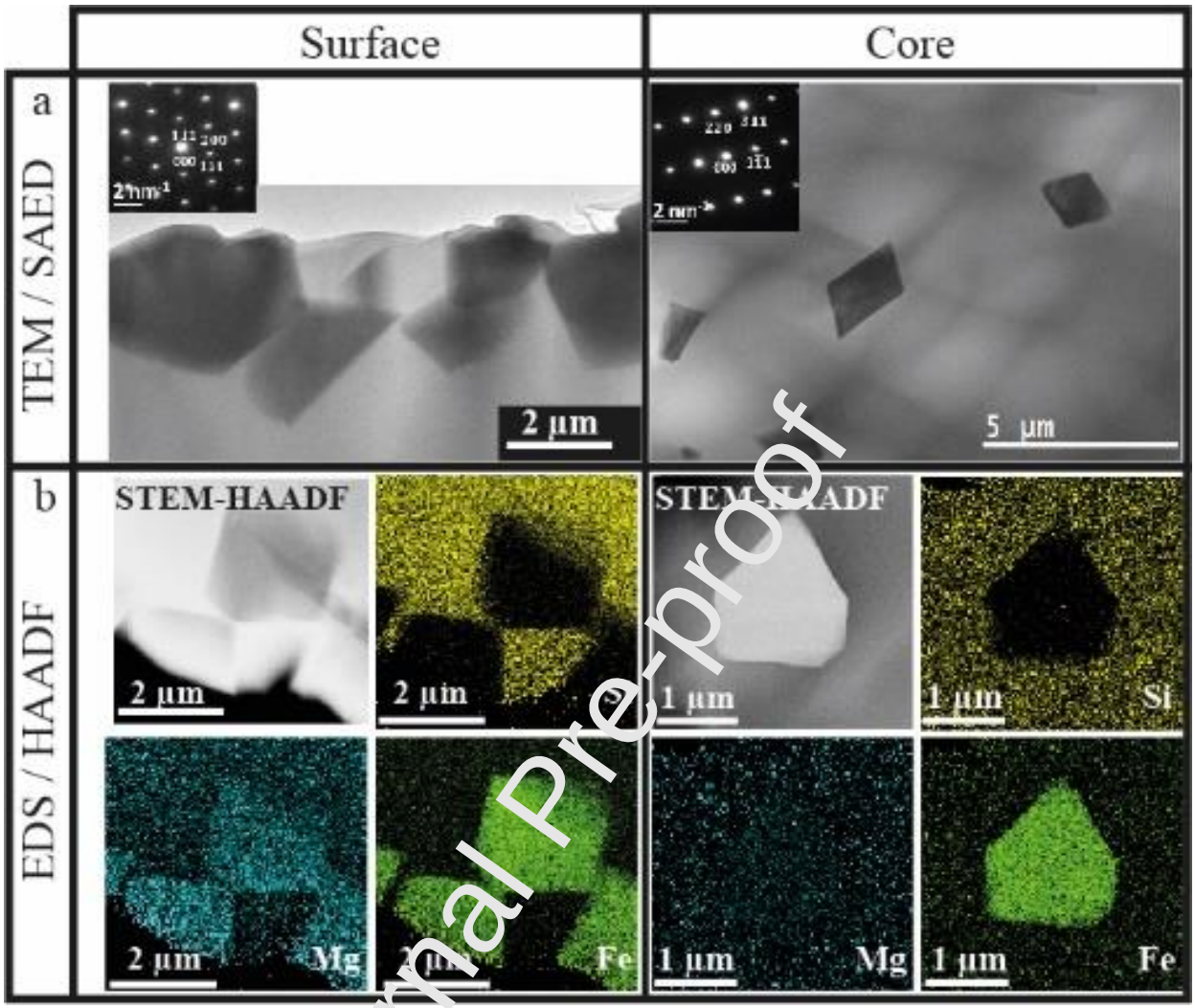


*Figure 6: a) Bright-field TEM micrographs illustrating the microstructure after IR of Bárðarbunga glass (B-glass) surface (left) and core (right). Inserts show example of SAED patterns in zone axis [011] and [112] for crystals situated at the surface and in the core, respectively. b) STEM-HAADF images associated with STEM-EDS elemental maps of Si (yellow), Mg (blue) and Fe (green). Note the contrast inversion in STEM-HAADF image for B-glass surface due to the sample thickness.*

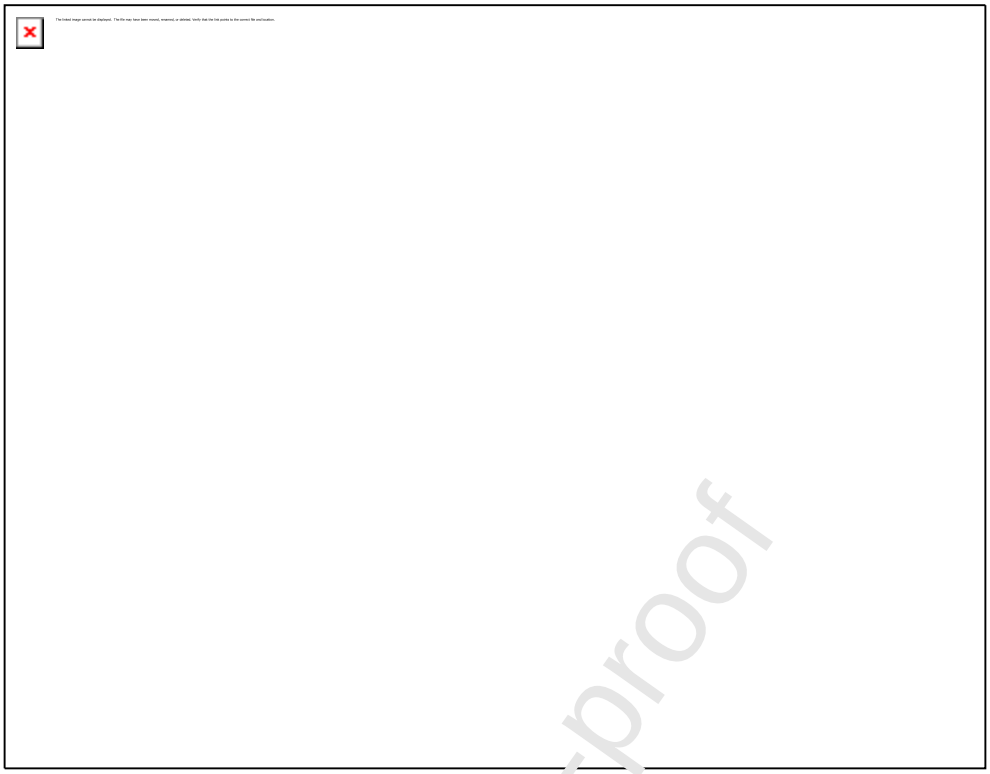

*Figure 7: DSC heating (plain lines) and cooling (dotted lines) curves of Bárðarbunga glass (B-glass) and Bárðarbunga Natural (B-Nat). Glass transition (917–939 K), and two crystallization events (1100–1132 K and 1270–1370 K) occur before melting (1416–1442 K).*

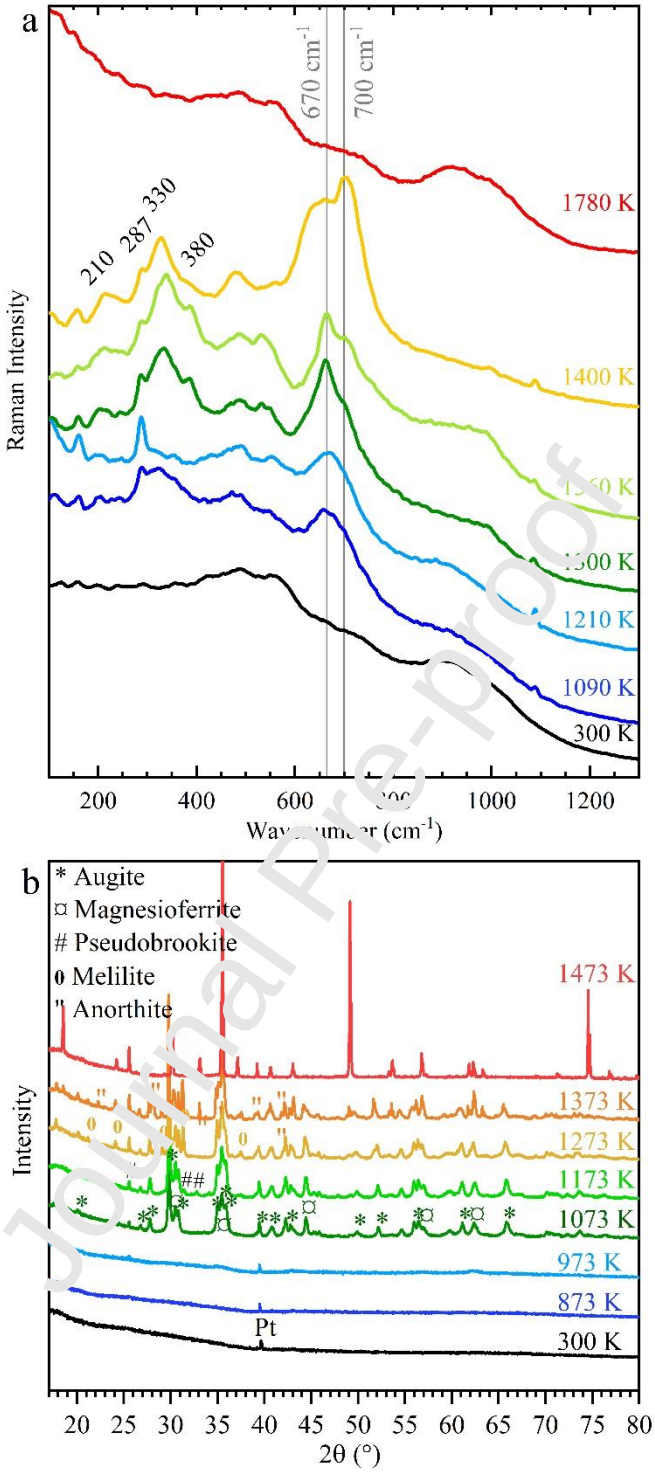


Figure 8: *Ex situ* Raman spectra of Bárðarbunga glass (B-glass) before (300 K, initial state) and after IR experiments (post mortem analysis at temperatures at which sample was quenched). Note that the two major bands at 670 and 700 $cm^{-1}$ are related to the vibration of Fe–O and the crystallization of clinopyroxene and Fe-Mg-rich oxides in the glass structure. The Raman spectra shown in raw state (arbitrary units) and stacked manner.
*b) In situ XRD diffractograms of B-glass microstructural evolution with temperature. The principal phases augite and magnesioferrite crystallize between 973 K and 1073 K. Note at low 2θ angles the characteristic feature of glass structure; Platinum (Pt) sample holder.*

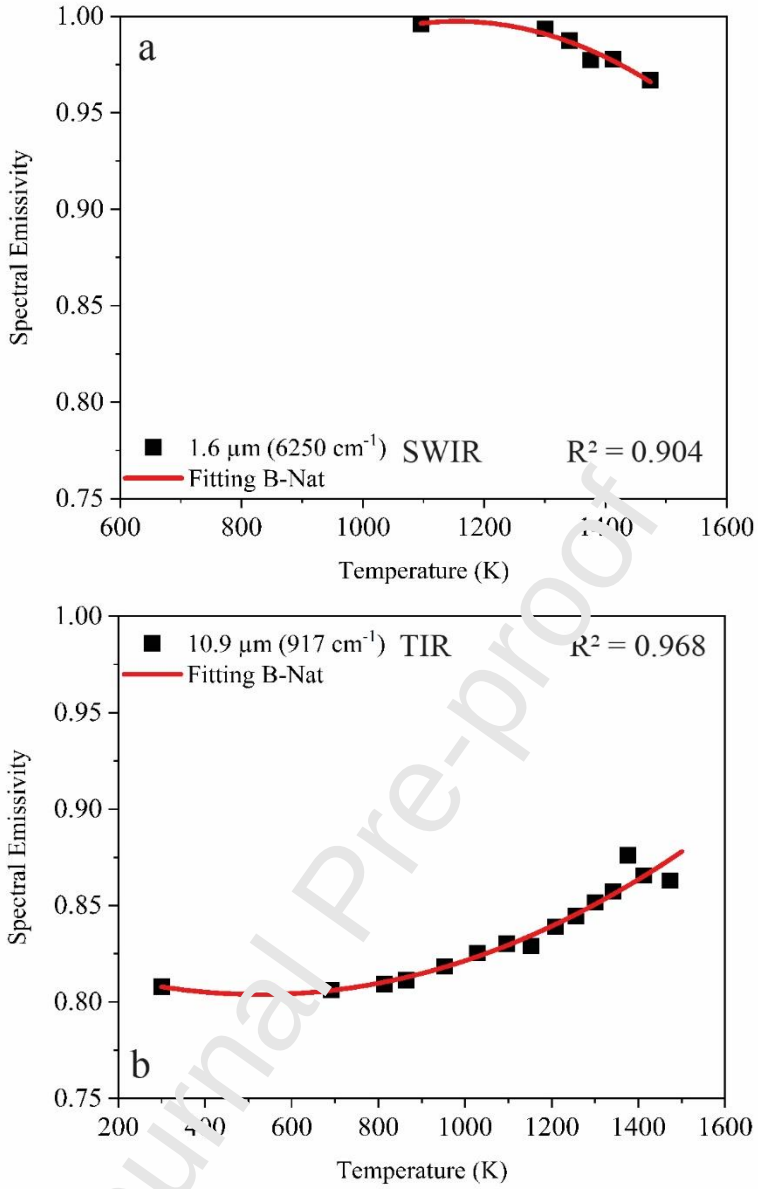


*Figure 9: Temperature evolution of spectral emissivity values in a) SWIR band 1.6 µm and b) TIR band 10.9µm for Piton de la Fournaise bunga Natural basalt that allows retrieving the equations of ε–T relationship at a given wavelength. Note that the sample must first reach higher temperature before emitting in SWIR, thus explaining the limited number of experimental data compared to TIR.*

Authors' contributions

JB: writing, original draft, data collection and analysis, investigation, methodology. AS: supervision, conceptualization, writing, funding acquisition. JA: supervision, conceptualization, writing, funding acquisition. LdC: writing, data analysis, review. LC: data collection, review. HL: review. EV: data collection and analysis, review. CG: data collection and analysis, review. SO: data collection and analysis, review. MA: data application, review.

**Declaration of interests**

☒The authors declare that they have no known competing financial interests or personal relationships that could have appeared to influence the work reported in this paper.

☐The authors declare the following financial interests/personal relationships which may be considered as potential competing interests:

Highlights

- Spectral emissivity data for basalts ranging from room temperature to 1800 K.
- Spectral emissivity data for basalts ranging from 350 to 8000 cm-1 (TIR-MIR-SWIR).
- Spectral emissivity increase with temperature in TIR and decreases in SWIR-MIR.
- Complex radiative properties due to crystallization and phase coexistence.
- Bárðarbunga–Holuhraun lava field temperature are refined by ~50 K.